Localized surface plasmon resonance-mediated fluorescence signals in plasmonic nanoparticle-quantum dot hybrids for ultrasensitive Zika virus RNA detection via hairpin hybridization assays

メタデータ	言語: eng
	出版者:
	公開日: 2018-12-07
	キーワード (Ja):
	キーワード (En):
	作成者: Adegoke, Oluwasesan, Morita, Masahiro, Kato, Tatsuya, Ito, Masahito, Suzuki, Tetsuro, Park, Enoch Y.
	メールアドレス:
	所属:
URL	http://hdl.handle.net/10297/00026136

Localized surface plasmon resonance-mediated fluorescence signals in plasmonic nanoparticle-quantum dot hybrids for ultrasensitive Zika virus RNA detection via hairpin hybridization assays

Oluwasesan Adegoke[a], Masahiro Morita[b], Tatsuya Kato[a,b,d], Masahito Ito[c], Tetsuro Suzuki[c], Enoch Y. Park[a,b,d*]

[a] *Laboratory of Biotechnology, Research Institute of Green Science and Technology, Shizuoka University, 836 Ohya, Suruga-ku, Shizuoka 422-8529, Japan*

[b] *Department of Applied Biological Chemistry, Shizuoka University, 836 Ohya, Suruga-ku, Shizuoka 422-8529, Japan*

[c] *Department of Virology and Parasitology, Hamamatsu University School of Medicine, 1-20-1 Higashi-ku, Handa-yama, Hamamatsu 431-3192, Japan*

[d] *Laboratory of Biotechnology, Graduate School of Science and Technology, Shizuoka University, 836 Ohya, Suruga-ku, Shizuoka 422-8529, Japan*

E-mail addresses:
adegoke.sesan@mailbox.co.za (OA)
nnndrum@yahoo.co.jp (MM)
kato.tatsuya@shizuoka.ac.jp (TK)
mito557@hama-med.ac.jp (MI)
tesuzuki@hama-med.ac.jp (TS)
park.enoch@shizuoka.ac.jp (EYP)

* Correspondence to: Research Institute of Green Science and Technology, Shizuoka University, 836 Ohya Suruga-ku, Shizuoka, 422-8529, Japan. Tel. & fax: +81 54 238 4887. *E-mail address:* park.enoch@shizuoka.ac.jp (EYP)

Abstract

The current epidemic caused by the Zika virus (ZIKV) and the devastating effects of this virus on fetal development, which result in an increased incidence of congenital microcephaly symptoms, have prompted the World Health Organization (WHO) to declare the ZIKV a public health issue of global concern. Efficient probes that offer high detection sensitivity and specificity are urgently required to aid in the point-of-care treatment of the virus. In this study, we show that localized surface plasmon resonance (LSPR) signals from plasmonic nanoparticles (NPs) can be used to mediate the fluorescence signal from semiconductor quantum dot (Qdot) nanocrystals in a molecular beacon (MB) biosensor probe for ZIKV RNA detection. Four different plasmonic NPs functionalized with 3-mercaptopropionic acid (MPA), namely MPA-AgNPs, MPA-AuNPs, core/shell (CS) Au/AgNPs, and alloyed AuAgNPs, were synthesized and conjugated to L-glutathione-capped CdSeS alloyed Qdots to form the respective LSPR-mediated fluorescence nanohybrid. The concept of the plasmonic NP-Qdot-MB biosensor involves using LSPR from the plasmonic NPs to mediate a fluorescence signal to the Qdots, triggered by the hybridization of the target ZIKV RNA with the DNA loop sequence of the MB. The extent of the fluorescence enhancement based on ZIKV RNA detection was proportional to the LSPR-mediated fluorescence signal. The limits of detection (LODs) of the nanohybrids were as follows: alloyed AuAgNP-Qdot646-MB (1.7 copies/mL)) > CS Au/AgNP-Qdot646-MB (LOD = 2.4 copies/mL) > AuNP-Qdot646-MB (LOD = 2.9 copies/mL) > AgNP-Qdot646-MB (LOD = 7.6 copies/mL). The LSPR-mediated fluorescence signal was stronger for the bimetallic plasmonic NP-Qdots than the single metallic plasmonic NP-Qdots. The plasmonic NP-Qdot-MB biosensor probes exhibited excellent selectivity toward ZIKV RNA and could serve as potential diagnostic probes for the point-of care detection of the virus.

1. Introduction

The history of Zika virus (ZIKV) dates back to 1947 when it was first isolated from a rhesus monkey in the East African country of Uganda and was named after the Zika forest, the geographical location where the virus was isolated **(Abushouk et al., 2016; Gebre et al., 2016; WHO, http://www.who.int/emergencies/zika-virus/timeline/en/).** The first reported occurrence of ZIKV infection in humans was reported in 1952 **(Macnamara, 1954)**, and within 60 years after the virus was first isolated, 13 cases of sporadic infection have been reported **(Fagbami, 1979; Moore et al., 1975; Olson et al., 1981).** The World Health Organization (WHO) declared on the 1st of February 2016 that Guillain-Barré syndrome and an increased incidence of congenital microcephaly were symptoms associated with ZIKV infection, thus raising an international public health concern **(WHO, http://www.who.int/mediacentre/news/statements/2016/emergency-committee-zika-microcephaly/en/).** In Brazil alone, approximately 1.5 million people have been estimated to be infected by the virus, and more than 20 countries have reported cases of ZIKV transmission **(Kinhauser et al., 2016; Lazear and Diamond, 2016).** The ZIKV is a single-stranded positive-sense RNA virus, which belongs to the *Flavivirus* genus of the *Flaviviridae* family **(Enfissi et al., 2016).** The virus can be transmitted sexually, from an infected mother to the fetus **(Calvet et al., 2016),** through day-time female *Aedes albopictus* and *Aedes aegypti* mosquito bites **(Sikka et al., 2016)** and through blood transfusion **(Marano et al., 2016).**

Current laboratory diagnostics for the ZIKV are primarily based on a serological analysis and a molecular diagnosis (reverse-transcriptase polymerase chain reaction (RT-PCR)). The serological analysis, which involves utilizing an enzyme-linked immunosorbent assay (ELISA)

to detect IgM antibodies in the serum sample, suffers from cross reactivity of antibodies among flaviviruses, thereby decreasing the specificity of the technique **(Gourinat et al., 2015; Lanciotti et al., 2008).** RT-PCR can detect ZIKV RNA at 530 aM (320 copies/µl) within a total assay time of 90 min **(Faye et al., 2013; Musso et al., 2014)**. However, due to the decrease in viremia over time, RT-PCR analysis is effective only during the onset of symptoms, which occurs in the first 7 days when the ZIKV load is at a level of ~1 fM in human fluid samples **(Barzon et al., 2016; Haug et al., 2016).** Beyond this time period, i.e., ≥ 4 days after symptom onset, reliable data can be obtained only via labor-intensive diagnoses **(Peterson et al., 2016).** With respect to the sensitivity of Zika RNA detection using RT-PCR, detection limits of 10^3 to 10^{11} copies/ mL (**Waggoner et al., 2016**), 140 copies viral RNA/reaction (**Balm et al., 2012**) and 0.05 pfu/mL (**Faye et al., 2013**) have been reported. In addition, a paper-based synthetic gene detection platform for ZIKV RNA was reported to exhibit a detection limit of 1.7 x 10^6 copies/mL (**Pardee et al., 2016**). The summarized detection limits suggests that improved sensitivity of ZIKV detection is still needed. Generally, there is an urgent need for the development of more efficient and reliable diagnostic probes for ZIKV that can alleviate the challenges of point-of-care testing for pregnant women, blood donors and travelers from regions with endemic transmission.

Biosensor probes that utilize the phenomenon of plasmonic signal transduction have emerged as useful alternatives for enhancing the sensitivity of detection platforms **(Adegoke et al., 2016b; Hall et al., 2011).** The exploitation of plasmonic metallic nanoparticles (NPs) in biosensing applications has been inspired by the interaction of these particles with electromagnetic waves, which induce oscillations of the plasmons (free electrons) at the particle surface **(Law et al., 2011)**. This phenomenon has led to the development of localized surface plasmon resonance (LSPR)-based biosensors for various analytes **(Anker et al., 2008; Hutter et al., 2003).** Exploiting LSPR signals to trigger the transduction of optical changes in

fluorescent semiconductor quantum dot (Qdot) nanocrystals within a molecular beacon (MB) biosensor probe for targeting an oligonucleotide sequence can be a unique strategy to construct ultrasensitive detection platforms for viral nucleic acids.

The phenomenon of hybridizing the loop sequence of an MB probe with the target nucleic acid sequence is reflected in the optical transduction changes in the reporter fluorophore. The ultrasensitive detection of the target nucleic acid sequence is dependent on the choice of reporter fluorophore. In this work, we developed four ultrasensitive LSPR-induced Qdot-MB biosensors for ZIKV RNA. ZIKV RNA was extracted, and the loop of the MB was designed to hybridize with the RNA of the virus genome. Four different plasmonic NPs, namely gold NPs (AuNPs), silver NPs (AgNPs), bimetallic core/shell (CS) Au/AgNPs and alloyed AuAgNPs, were synthesized and functionalized with 3-mercaptopropionic acid (MPA). Each of the MPA-functionalized plasmonic NPs was bonded to L-glutathione (GSH)-capped CdSeS alloyed Qdots to form novel fluorescent nanohybrid systems, which were subsequently conjugated to an MB and utilized as ultrasensitive LSPR-fluorescence signal transducers for ZIKV RNA detection. Optical engineering of the alloyed CdSeS Qdots ensured the appropriate selection of the Qdot size based on the photoluminescence (PL) quantum yield (QY) value. Our MB biosensor platform shows that each of the plasmonic NPs can induce LSPR signals to trigger ultrasensitive fluorescence transduction changes in the alloyed Qdots for the detection of extremely low concentrations of ZIKV RNA. Notably, the extent of the LSPR-fluorescence signal enhancement was dependent on the plasmonic nanostructure, with the bimetallic NPs triggering a higher LSPR-fluorescence signal intensity than the single metallic plasmonic NPs. Our work is the first to construct an ultrasensitive LSPR-mediated fluorescence Qdot-MB biosensor for ZIKV RNA.

2. Materials and methods

2.1. Materials

Cadmium oxide (CdO), trioctylphosphine (TOP), octadecene (ODE), hexadecylamine (HDA), trioctylphosphine oxide (TOPO), selenium (Se), $HAuCl_4 \cdot 3H_2O$, sulfur (S), rhodamine 6G, MPA, GSH, tannic acid, silver nitrate ($AgNO_3$), N-(3-dimethylaminopropyl)-N′-ethylcarbodiimide hydrochloride (EDC) and N-hydroxysuccinimide (NHS) were purchased from Sigma Aldrich Co. LLC (Saint Louis, MO, USA). Oleic acid (OA) was purchased from Nacalai Tesque Inc. (Kyoto, Japan). Potassium hydroxide (KOH), methanol, tri-sodium citrate, acetone and chloroform were purchased from Wako Pure Chemical Ind. Ltd. (Osaka, Japan). Norovirus RNA of genogroup II (G11) was purchased from Vircell Microbiologists (Granada, Spain). Clinically isolated influenza virus A/Yokohama/110/2009 (H3N2) was supplied by Dr. C. Kawakami of the Yokohama City Institute of Health, Japan. ZIKV strain PRVABC-59 was kindly provided by Professor Kouichi Morita of Institute of tropical medicine Nagasaki University. The ZIKV sample was obtained from culture supernatant that was collected from African green monkey kidney-derived Vero cells infected with ZIKV. Due to the absence of ZIKV outbreak in Japan and because only a few reported ZIKV-positive cases introduced from people from other countries to date, it is however quite difficult to obtain virus samples from infected patients. However, we can expect no possible drawback in the case of clinical samples, such as patients' sera because total RNAs are only extracted from human sera as efficiently as those from cell-culture supernatants according to the RNA isolation protocol used in this study.

An ultrapure Milli-Q water system was used for sample preparation. The MB with a loop sequence specific for the target ZIKV RNA was synthesized and purified via HPLC by FASMAC (Kanagawa, Japan). The loop of the MB was composed of a 23-bp single-stranded DNA with the 5' terminus labeled with an amino group (NH_2) and the 3' terminus conjugated

to the fluorescence quencher 4-((4-(dimethylamino)phenyl)azo)benzoic acid (dabcyl). The MB oligonucleotide sequence is as follows:

5'-/NH$_2$-/**GCGAC**CACGGGCTACTCCGCGTTTTAGC**GTCGC**-dabcyl/-3'.

The stem domain is indicated by the underlined sequence.

The sequence of the ZIKV RNA targeted is: GCTAAAACGCGGAGTAGCCCGTG. This target sequence is conserved in ZIKV strains and doesn't match with the closely related *Flavivirus* species.

2.2. Equipment

Fluorescence emission measurements and UV/vis absorption were performed using a filter-based multimode microplate reader (Infinite® F500, TECAN, Ltd., Männedorf, Switzerland). Powder X-ray diffraction (PXRD) measurements were obtained using a RINT Ultima XRD instrument (Rigaku Co., Tokyo, Japan) with a Ni filter and a Cu-Kα source. The data were collected from 2theta = 5–90° at a scan rate of 0.01°/step and 10 s/point. Transmission electron microscopy (TEM) images were captured using a TEM (JEM-2100F, JEOL, Ltd., Tokyo, Japan) operated at 100 kV. Dynamic light scattering (DLS) and zeta potential (ZP) measurements were performed using a Zetasizer Nano series. Data analysis was performed using the Malvern Instrument Dispersion Technology software (version 7.1).

2.3. Synthesis of MPA-capped plasmonic NPs

AuNPs, AgNPs, bimetallic CS Au/AgNPs and alloyed AuAgNPs were synthesized by first capping the particles with citrate, and then a ligand exchange reaction to functionalize their surfaces with MPA was carried out. Citrate-capped AuNPs were synthesized by mixing 1 mL of 1% HAuCl$_4$·3H$_2$O solution with 79 mL of water, to which a citrate solution containing 4 mL of 1% tri-sodium citrate mixed with 0.5 mL of tannic acid and 15.5 mL of ultrapure

deionized water was added **(Slot and Gueza, 1988)**. The solution was stirred for a few minutes and heated to ~60 °C. This procedure resulted in the formation of citrate-capped AuNPs. To form the citrate-capped AgNPs, the 1% $HAuCl_4 \cdot 3H_2O$ solution was replaced with 1% $AgNO_3$, and the same procedure was followed. To form the bimetallic alloyed AuAgNPs, 1 mL each of 1% $HAuCl_4 \cdot 3H_2O$ and 1% $AgNO_3$ were mixed together in the same synthesis pot, and the same procedure (as described above) was followed. To form the bimetallic CS Au/AgNPs, separate solutions of citrate-AuNPs and citrate-AgNPs were synthesized, and 50 mL of citrate-AuNPs was coated around 50 mL of citrate-AgNPs solution by mixing together and stirring for a few minutes.

Ligand exchange reactions involving the replacement of citrate with MPA were performed via a KOH-methanolic-MPA solution **(Adegoke et al., 2016).** Briefly, 3 g of KOH was dissolved in 40 mL of methanol, 2 mL of MPA was then added followed by stirring. Separate solutions (50 mL each) of citrate-capped AuNPs, AgNPs, bimetallic CS Au/AgNPs and alloyed AuAgNPs were added to separate KOH-methanolic-MPA solutions and stirred for a few minutes. The plasmonic NPs were purified by centrifugation at $1500 \times g$ for 10 min and subsequently dissolved in ultrapure deionized water. The plasmonic NP solutions were stored at 4 °C prior to use.

2.4. Synthesis of GSH-CdSeS alloyed Qdots

The synthesis of alloyed CdSeS Qdots was carried out via the organometallic hot-injection synthesis route, and a ligand exchange reaction was employed to convert the hydrophobic Qdots to water-soluble Qdots. To obtain varied sizes of Qdots, optical engineering of the Qdots was carried out. The synthesis approach carried out in this work was a modified strategy previously reported in the literature **(Adegoke et al., 2015a).** Prior to the synthesis, trioctylphosphine selenide (TOPSe) was prepared by mixing 60 mg of Se with 5 mL of TOP,

whereas the TOPS precursor was prepared by mixing 80 mg of S with 1.93 g of TOPO, 1 mL of TOP, 10 mL of ODE and 5 mL of OA. Under an Ar gas flow, 0.4 g of CdO was mixed with 1.93 g of TOPO, 1.0 g of HDA, 20 mL of ODE and 15 mL of OA and then heated. At an elevated temperature, precursor solutions of TOPSe and TOPS were added simultaneously to generate the alloyed CdSeS Qdots. The temperature of the solution was varied from ~260 °C to 300 °C to tune the size of the Qdots. Four sizes of the hydrophobic CdSeS Qdots were harvested at different time intervals and purified with methanol followed by acetone.

The ligand exchange with GSH was carried out by adding hydrophobic Qdot solutions (in chloroform) to separate KOH (3 g)-methanolic (40 mL)-GSH (2 g) ligand solutions and stirring for a few minutes. The GSH-functionalized Qdots were purified using acetone, chloroform and an acetone/chloroform mixture. Based on their PL emission wavelength, the four different-sized Qdot nanocrystals were denoted as Qdot568, Qdot590, Qdot610 and Qdot646.

2.5. Preparation of the plasmonic NP-Qdot-MB bioprobe (Scheme 1)

The GSH-Qdot646 was selected as the reporter fluorophore signal in this study based on its superior optical properties. The plasmonic MPA-capped AgNPs, AuNPs, bimetallic CS Au/AgNPs and alloyed AuAgNPs were conjugated to GSH-Qdot646 to form four different plasmonic NP-Qdot nanohybrids. Briefly, 2 mL of each aqueous plasmonic NP (0.05 µM) solution in ultrapure Millipore water was mixed separately with 500 µL of 0.1 M EDC to activate the terminal carboxylic groups. After stirring for ~1 hr, 2 mL of an aqueous solution of Qdot646 (1 mg/mL) was added immediately followed by the addition of 500 µL of NHS. The solution was left to react until the next day and purified via centrifugation at $1500 \times g$ for 3 min using a Nanosep® centrifugal filter (Pall Co., Port Washington, NY, USA) with a 30,000 Microcon molecular weight cut-off.

Following the conjugation of the plasmonic NPs to Qdot646 particles, AgNP-Qdot646, AuNP-Qdot646, CS Au/AgNP-Qdot646 and alloyed AuAgNP-Qdot646 nanohybrids were formed. Each of the nanohybrids was conjugated to the MB to form the LSPR-mediated fluorescence Qdot biosensor probes to be used for ZIKV RNA detection. A purified aqueous solution of each plasmonic NP-Qdot nanohybrid (2 mL) was mixed with 500 µL each of EDC, NHS and the MB (0.5 nmol) solution and stirred for ~1 hr. The plasmonic NP-Qdot-MB conjugates thus formed were purified as described above for the plasmonic NP-Qdot nanohybrids.

2.6. Total RNA extraction

The isolation of total RNA was carried out using a commercial genomic RNA extraction procedure detailed in the High Pure Viral Nucleic Acid Kit by Roche Diagnostics GmbH (Mannheim, Germany). Briefly, 200 µL of the ZIKV sample was mixed with 200 µL of a binding buffer supplemented with poly[A] carrier RNA and proteinase K. The solution was incubated at 72 °C, mixed with binding buffer and then centrifuged for 1 min at 8000 $\times$ g. Inhibitor removal buffer, wash buffer and elution buffer were each added at different stages with repeated centrifugation. The extracted ZIKV RNA was collected in a tube and stored at -30 °C prior to use. The RNA of the clinically isolated influenza virus H3N2 was also extracted using this protocol. The extracted influenza virus H3N2 RNA was used as a negative control to test the specificity of the biosensor probe toward ZIKV RNA.

2.7. Quantification of ZIKV RNA

Copies of ZIKV RNA were determined by quantitative RT-PCR in an CFX Connect Real-Time System (Bio Rad, Hercules, CA). The 3'UTR sequences of ZIKV were chosen as target for the primers. ZIKV strains from the African founder strain (MR766, accession number

LC002520) and a Puerto Rico strain (PRVABC59, accession number KX087101) were aligned using the Clustal W program (**Thompson et al., 1997**). A stretch of nucleotides conserved in the strains was identified and the primers and a probe sequence were designed. The assay probe was ZEN double-quenched probe, which include an internal ZEN quencher, a 3' Iowa Black forward quencher (IABkFQ), and a 5' 6-FAM reporter (Integrated DNA Technologies,. Coralville, Iowa, USA). The primer–probe set consists of the 5'-GGGACTAGTGGTTAGAGGAGAC-3' forward primer, 5'-CAGCGTGGTGGAAACTCAT-3' reverse primer, and 5'-6-FAM-AGCATATTG-ZEN-ACGCTGGGAAAGACCA-IABkFQ-3' probe. The Taqman Fast virus 1-step master mix (Thermo Fisher Scientific, Rockford, IL) was used with a 10 μL reaction mixture under the following conditions: 3.125 μL of kit enzyme mixture (including thermostable moloney murine leukemia virus (MMLV)-RT and AmpliTaq Fast DNA Polymerase), 6.25×10^{-2} μL of 100 μM of each primer, 2.5×10^{-2} μL of 100 μM of probe, 6.725 μL of RNase free water and 2.5 μL of the extracted sample. The following thermal profile was used a single cycle of reverse transcription for 5 min at 50 °C, 20 sec at 95 °C for reverse transcriptase inactivation and DNA polymerase activation followed by 45 amplification cycles of 3 sec at 95 °C and 30 sec 60 °C. Standard curves were generated from serial dilutions of the nucleic acid extracted from virus stocks ranging from 10^2 to 10^8 copies/μL where 100 copies was the limit of detection. The concentration of the stock ZIKV RNA was measured as 1.2×10^8 copies/mL.

2.7. LSPR-mediated fluorescence Qdot-MB assay

The LSPR-mediated fluorescence Qdot-MB detection assay was carried out in a 96-well plate by mixing 2 μL of the plasmonic NP-Qdot-MB probe solution with 43 μL of a Tris-EDTA buffer and 5 μL of the target ZIKV RNA. A hybridization time of 3 min was allowed,

and the fluorescence measurement was carried out in the wavelength range of 480-800 nm with an excitation wavelength of 470 nm.

2.8. LSPR-mediated fluorescence Qdot-MB detection principle

Scheme 1 displays a schematic description of the detection principle of the LSPR-mediated fluorescence Qdot-MB biosensor. First, each type of plasmonic NP was conjugated to Qdot646 nanocrystals to form the respective plasmonic NP-Qdot646 nanohybrid, which was then conjugated to the 5' end of the MB. In the absence of the target ZIKV RNA, the MB maintains a hairpin stem-loop structure with the dabcyl quencher in close proximity to the plasmonic NP-Qdot reporter fluorophore. At this stage, the fluorescence of the plasmonic NP-Qdot fluorophore is quenched. Upon hybridization of the target ZIKV RNA with the DNA loop sequence of the MB, an RNA/DNA heteroduplex is formed, and the fluorescence enhancement signal is triggered based on the LSPR signal from the bonded plasmonic NPs to the Qdot fluorophore. The extent of the fluorescence enhancement of the Qdot signal is dependent on the strength of the LSPR signal from the plasmonic NPs and thus equivalent to the concentration of the target ZIKV RNA.

3. Results and discussion

3.1. Optical properties of the plasmonic NPs and Qdots

3.1.1. Plasmonic NPs

The optical properties of the plasmonic NPs were characterized by UV/vis absorption spectrophotometry. Fig. 1 A shows the UV/vis absorption spectra of the MPA-capped AuNPs, AgNPs, CS Au/AgNPs and alloyed AuAgNPs. The position of the SPR peak in the absorption spectra of the NPs clearly occurs at different absorption wavelengths. The absorption spectra of the AuNPs and alloyed AuAgNPs have an SPR peak maximum value at 538 nm, and that of

the AgNPs is at 422 nm, whereas the CS Au/AgNPs have prominent SPR peaks at 424 nm and a broad SPR peak between 538 and 560 nm. It should be noted that the SPR absorption wavelength of the respective NPs is dependent on their structure and size. Generally, the SPR peaks of the MPA-AgNPs and AuNPs are in good agreement with those in the literature **(Chen et al., 2006; Li et al., 2010).** A comparison of the absorption spectra between the alloyed AuAgNPs and the CS Au/AgNPs reveals differences in their SPR peak positions as a result of the synthesis process. To form the CS structure, AuNPs and AgNPs were synthesized separately and mixed together in the same synthesis pot, whereas the precursor solutions of Au and Ag were used in the same synthesis pot to simultaneously form the alloyed AuAgNPs. The effect of the synthesis process results in an SPR peak attributed to the AgNPs at 424 nm and a broad SPR peak attributed to the AuNPs at 538–560 nm, thus indicating the formation of the CS Au/AgNPs. Conversely, a single SPR peak was displayed for the alloyed AuAgNPs.

3.1.2. Size-dependent Qdots

Optical engineering of the alloyed Qdots was carried out to obtain different sizes. The advantage of such a fabrication technique ensures that the optical properties of the Qdots can be tuned across a broad PL emission wavelength range, thus providing the ability to select the appropriate Qdot fluorophore. Fig. 1B and C show the evolution of the absorption and PL emission spectra of the different-sized GSH-capped CdSeS alloyed Qdots. The corresponding absorption wavelength maximum values for the different Qdot sizes were 558 nm for GSH-Qdot568, 580 nm for GSH-Qdot590, 600 nm for GSH-Qdot610 and 606 nm for GSH-Qdot646. Tuning the PL emission wavelength of the Qdots from 568 nm to 646 nm reflects the quantum size characteristics of the Qdots. The quality of each Qdot size was assessed using rhodamine 6G dissolved in ethanol as a reference standard ($\Phi_{Fl}^{R6G} = 0.95$) and determining the PL QY according to the following equation:

$$\Phi_{Fl}^{QD} = \Phi_{Fl}^{R6G} \frac{F_l^{QD} \cdot OD_{R6G(\lambda exc)} \cdot n_{water}^2}{F_l^{R6G} \cdot QD_{QD(\lambda exc)} \cdot n_{ethanol}^2}$$

where Φ_{Fl}^{Qdot} is the PL QY of the Qdots, Φ_{Fl}^{R6G} represents the PL of the standard, F_l^{R6G} and F_l^{QD} are the integrated sums of the PL intensity of the standard and the Qdots, respectively, $OD_{QD(\lambda exc)}$ and $OD_{R6G(\lambda exc)}$ are the optical densities of the Qdots and the rhodamine standard, respectively, at the excitation wavelength of 470 nm for the former and 400 nm for the latter, and $n_{ethanol}^2$ and n_{water}^2 are the refractive indexes of the solvents used to dissolve the standard and the Qdots. The corresponding PL QY values of the Qdots are 6% for GSH-Qdot568, 9% for GSH-Qdot590, 46% for GSH-Qdot610 and 97% for GSH-Qdot646. From the values of the PL QY of the alloyed Qdots, it is clearly evident that as the PL emission wavelength based on size shifted to the red region, the PL QY increased. This result implies that the PL QY of the Qdots is dependent on the Qdot size. A general concept in luminescent Qdot technology considers that the lower the Qdot PL QY, the higher the surface defect state and the lower the sensitivity of the Qdots and vice versa. This phenomenon implies that dangling bonds that act as surface traps on the surface of the Qdots are suppressed as the PL QY of the Qdots increases. Based on the PL QY analysis of our Qdots, we can generally infer that the extent of the interfacial surface defect state decreased as the size of the Qdots increased. Therefore, for our biosensor application, GSH-Qdot646 nanocrystals were selected as the reporter fluorophore due to the higher PL QY.

3.2. Structural properties of the plasmonic NPs and Qdots

3.2.1. TEM

The TEM images of the plasmonic NPs and the selected Qdot646 nanocrystals are shown in Fig. 2A–E. The TEM images of the other Qdot sizes are shown in Fig. S-1 (Supplementary Information). Fig. 2A and B display the TEM images of the MPA-capped AgNPs and the

AuNPs, respectively, whereas Fig. 2C, D and E show the CS Au/AgNPs, alloyed AuAgNPs, and GSH-capped Qdot646 particles, respectively. According to the TEM monograph, the AgNPs are relatively spherical with a heterogeneous particle size distribution. The AuNPs displayed a monodisperse particle size distribution with a consistent spherical morphology. The bimetallic CS Au/AgNPs displays a relatively quasi-type of shape morphology due to the core/shell formation. Alloyed AuAgNPs exhibited spherical shape morphologies and moderate particle size monodispersity. For the GSH-Qdot646 particles, a quasi-spherical shape pattern was exhibited, thus indicating a heterogeneous nucleation of the nanocrystals. The corresponding particle size distribution histograms are shown in Fig. 2A1–E1, and the size values obtained were 7.8 ± 3.0 nm for the MPA-AgNPs, 2.7 ± 0.6 nm for the MPA-AuNPs, 4.4 ± 0.6 nm for the CS MPA-Au/AgNPs, 2.9 ± 1.1 nm for the alloyed MPA-AuAgNPs and 4.3 ± 2.7 nm for the GSH-Qdot646 nanocrystals.

3.2.2. PXRD

The crystal structures of the plasmonic NPs and the Qdots were analyzed using PXRD. The size of the NPs is reflected in the nature of their diffraction patterns as depicted in Fig. 3A. Ideally, smaller-sized NPs are expected to exhibit broader diffraction peaks and vice versa. Clearly, the MPA-capped AgNPs and CS Au/AgNPs exhibit narrower diffraction peaks than the AuNPs and alloyed AuAgNPs due to their larger particle size. The diffraction patterns of the NPs were effectively indexed to the {111}, {200}, {220} and {311} planes, respectively, and these results tentatively confirmed the crystalline structure of these NPs. The diffraction peaks of the MPA-AgNPs and CS Au/AgNPs were indexed to the face-centered cubic (fcc) crystalline structure of Ag with respect to the JSPDS file No. 04-0783 **(Khan et al., 2011),** whereas those of the AuNPs and alloy AuAgNPs were indexed to the fcc crystalline structure of Au with respect to the JCPDS file No. 04-0784 **(Sharma and Rabinal, 2015).**

The XRD spectra of the selected GSH-Qdot646 particles are shown in Fig. 3B; the corresponding XRD spectra for the other Qdot sizes are depicted in Fig. S-2 (Supplementary Information). Based on Fig. 3B, the diffraction pattern of the Qdots corresponds to a zinc-blende crystal structure with the peaks indexed to the {111}, {220} and {311} planes. The narrow diffraction peak of the Qdot646 particles is due to the larger nanocrystalline size of these particles. The diffraction peaks of the Qdots were indexed to the JCPDS file No. 19-0191 for CdSe QDs **(Pan et al., 2007).**

3.2.3. DLS and ZP

When particles within a colloidal dispersion scatter incident light, the scattered light intensity can be detected and measured by DLS, and this technique can be used to measure the hydrodynamic size of the particle. Theoretically, colloidal NP dispersions scatter incident light in proportion to the 6th power of the NP radius **(Rademeyer et al., 2015).** DLS is a powerful tool that provides better robust data regarding the particle size distribution and can be used to probe for NP agglomeration as a function of the aqueous solution used for suspension. Ideally, for a monodisperse and non-agglomerated NP dispersion, the hydrodynamic data will be less than 100 nm or closer to the TEM particle size value. However, for a polydisperse and agglomerated NP dispersion, the hydrodynamic size will be in the range of 100–300 nm. The hydrodynamic particle size distribution plots for the plasmonic NPs and the GSH-Qdot646 particles are shown in Fig. 4A–E, and the values obtained were 22.5 ± 7.4 nm for the MPA-AgNPs, 12.4 ± 4.5 nm for the MPA-AuNPs, 22.5 ± 7.2 nm for the CS MPA-Au/AgNPs, 21.6 ± 6.9 nm for the alloyed MPA-AuAgNPs and 20.8 ± 9.9 nm for the GSH-Qdot646 particles. The hydrodynamic particle size values obtained for the plasmonic NPs and Qdots are less than 100 nm, thus confirming their monodisperse nature and non-agglomerated state.

The electrokinetic potential, also termed ZP, is the potential at the shear/slipping plane of a NP colloidal dispersion solution under the influence of an electric field. The ZP indicates the potential difference between the layer of a dispersant around an electrophoretically mobile NP at the slipping surface and the electric double layer of an electrophoretically mobile NP (**Kaszuba et al., 2010**). The ZP is a powerful parameter used in pharmaceutics and by colloidal chemists to characterize the colloidal stability of NPs in solution. The general guidelines used are as follows: highly unstable (±0–10 mV), relatively stable (±10–20 mV), moderately stable (±20–30 mV) and highly stable (±30 mV) (**Patel et al., 2011**). The ZP plots for the plasmonic NPs and the Qdot646 particles are shown in Fig. 4A1–E1, and the corresponding values obtained were -54.6 ± 14.4 mV for the MPA-AgNPs, -58.7 ± 9.2 mV for the MPA-AuNPs, -51.1 ± 13.5 mV for the CS MPA-Au/AgNPs, -46.9 ± 10.2 mV for the alloyed MPA-AuAgNPs and -52.7 ± 10.7 mV for the Qdot646 particles. The ZP values obtained for the plasmonic NPs and Qdot646 particles were within the high colloidal stability range.

3.3. Plasmonic NP-Qdot and plasmonic NP-Qdot-MB characterization

The TEM images of the plasmonic NP-Qdot nanohybrids are shown in Fig. 5A–D. Comparing the morphology of the AgNP-Qdot646 (Fig. 5A), AuNP-Qdot646 (Fig. 5B), CS Au/AgNP-Qdot646 (Fig. 5C) and alloyed AuAgNP-Qdot646 nanohybrids (Fig. 5D), the coarse morphology of the particles clearly reflects the strong binding of the Qdots to the plasmonic NPs. The structural features of both the Qdots and plasmonic NPs are well defined in the respective TEM monographs. The TEM images of the plasmonic NP-Qdot-MB conjugates (Fig. 5A1–D1) exhibit similarities with the plasmonic NP-Qdot nanohybrids. In fact, the TEM images of the CS Au/AgNP-Qdot646-MB (Fig. 5C1) and alloyed AuAgNP-Qdot646-MB (Fig. 5D1) reveal a more refined, monodisperse particle morphology. We can tentatively confirm

that the structural features of the plasmonic-Qdot nanohybrids were not distorted upon binding to the MB.

DLS was used to characterize the particle size distribution and dispersity of the plasmonic NP-Qdot nanohybrids and the plasmonic NP-Qdot-MB probes, whereas the ZP measurements were used to characterize their corresponding colloidal stability. Fig. S-3A–D (Supplementary Information) shows the DLS plots for the plasmonic NP-Qdot nanohybrids, and Fig. S-3A1–D1 displays the corresponding ZP plots. The hydrodynamic size and ZP values obtained for the plasmonic NP-Qdot nanohybrids were, respectively, 22.5 ± 7.4 nm and -34.2 ± 8.9 mV for the AgNP-Qdot646 nanohybrid, 81.2 ± 20.9 nm and -28.7 ± 4.5 mV for the AuNP-Qdot646 nanohybrid, 95.8 ± 67.9 nm and -32.5 ± 3.4 mV for the CS Au/AgNP-Qdot646 nanohybrid and 196.2 ± 27.5 nm and -27.8 ± 3.5 mV for the alloyed AuAgNP-Qdot646 nanohybrid. Based on the hydrodynamic size values obtained, the monodispersity of the plasmonic-Qdot nanohybrids corresponded to the following order: AgNP-Qdot646 > AuNP-Qdot646 > CS Au/AgNP-Qdot646 > alloyed AuAgNP-Qdot646. These results indicate that the bimetallic-NP-Qdot nanohybrids exhibited a higher polydispersity index than the single metallic NP-Qdot nanohybrids. With respect to colloidal stability, the AgNP-Qdot646 and CS Au/AgNP-Qdot646 were highly stable, whereas the AuNP-Qdot646 and alloyed AuAgNP-Qdot646 were moderately stable. A discussion on the hydrodynamic size and ZP values of the plasmonic-NP-Qdot-MB probes is presented in Supplementary Information (Fig. S4).

Fig. 6A indicates that the PL quenching effects of the plasmonic NPs on the fluorescence intensity of the Qdot646 particles occurred to varying degrees. The magnitude of the quenching effect of the plasmonic NPs on the Qdot fluorescence occurred in the following order: AgNPs > CS Au/AgNPs > alloyed AuAgNPs > AuNPs. The degree of quenching may be attributed to the structural nature of the NPs.

3.4. Detection of ZIKV RNA

We carried out a hybridization time-lapse study to probe the fluorescence intensity signal of the LSPR-mediated fluorescence Qdot-MB probe upon interaction with the target ZIKV RNA. Fig S-5 (Supplementary Information) shows the fluorescence intensity signal as a function of time for the detection of 673 copies/mL of ZIKV using alloyed AuAgNP-Qdot646-MB (used as a representative). A sharp increase in fluorescence intensity signal was observed at 3 min and a steady decline was observed thereafter. For this work, a 3 min hybridization time was selected. The detection of ZIKV RNA was carried out with the respective plasmonic NP-Qdot-MB biosensor probes. We challenged the four plasmonic NP-Qdot-MB biosensor probes to detect ultrasmall concentrations of ZIKV. Fig. 6 shows the fluorescence enhancement effect of the AgNP-Qdot646-MB (Fig. 6B), AuNP-Qdot646-MB (Fig. 6C), CS Au/AgNP-Qdot646-MB (Fig. 6D), and alloyed AuAgNP-Qdot646-MB probes (Fig. 6E) in the detection of ZIKV based on the hybridization of the virus RNA with the DNA loop sequence of the probe. The AgNP-Qdot646-MB and CS Au/AgNP-Qdot646-MB probes detected ZIKV RNA in the concentration range of 6.73–6730 copies/mL, whereas the AuNP-Qdot646-MB and alloyed AuAgNP-Qdot646-MB probes detected ZIKV in the concentration range of 6.73–673 copies/mL.

The magnitude of the LSPR-mediated fluorescence was proportional to the concentration of the ZIKV RNA, thus determining the sensitivity of the biosensor probe. The corresponding fluorescence calibration curves are shown in Fig. 7A–D, in which the limit of detection (LOD) was calculated by multiplying the standard deviation values of the blank measurements (n = 10) by three and then dividing by the slope of the calibration curve. The LOD values obtained were in the following order: alloyed AuAgNP-Qdot646-MB (LOD = 1.7 copies/mL)) > CS Au/AgNP-Qdot646-MB (LOD = 2.4 copies/mL); AuNP-Qdot646-MB (LOD = 2.9 copies/mL) > AgNP-Qdot646-MB (LOD = 7.6 copies/mL). We found that each of the plasmonic NP-Qdot-

MB biosensor probes detected low concentrations of ZIKV RNA. However, the degree of the detection sensitivity varied among the bioprobes, with the bimetallic plasmonic NP-Qdots able to induce stronger LSPR signals in the Qdots than the single metallic plasmonic NP-Qdots. This result implies that the structural nature of the plasmonic NPs influences their LSPR effect.

To prove that the LSPR effect influenced the fluorescence signal for detecting ZIKV RNA, we performed a control study in which Qdot646 particles were directly conjugated to the MB without the LSPR effect from the plasmonic NPs, and the Qdot646-MB thus formed was utilized to detect ZIKV. Fig. S-6 (Supplementary Information) shows the fluorescence quenching effects of 673 copies/mL and 6730 copies/mL ZIKV RNA on the fluorescence of the Qdot646-MB probe. The quenched fluorescence signal indicated that the Qdot646-MB probe could not detect ZIKV RNA at these concentrations. These results therefore imply that the LSPR signal from the plasmonic NPs did indeed influence the fluorescence signal of the Qdots in detecting low concentrations of ZIKV RNA with the MB probe.

3.5. Specificity of the plasmonic NP-Qdot-MB biosensor

The specificity of the plasmonic NP-Qdot-MB biosensor probes for ZIKV was investigated by testing the efficacy of detecting the clinically isolated influenza virus H3N2 RNA and norovirus GII RNA. Fig. 8A–D compares the effect of the negative control on the fluorescence signal to that of the target ZIKV RNA on the fluorescence of the plasmonic NP-Qdot-MB biosensor probes. With both the influenza virus H3N2 RNA and norovirus RNA, the fluorescence remained quenched in the respective plasmonic NP-Qdot-MB biosensor probes, thus indicating their non-specificity regarding the biosensor. We can emphatically conclude that each of the plasmonic NP-Qdot-MB biosensor probes, the AgNP-Qdot646-MB (Fig. 8A), AuNP-Qdot646-MB (Fig. 8B), CS Au/AgNP-Qdot646-MB (Fig. 8C) and alloyed AuAgNP-Qdot646-MB (Fig. 8D), specifically detected ZIKV RNA.

4. Conclusion

We designed four novel plasmonic NP-Qdot-MB biosensor probes for ZIKV RNA based on LSPR-mediated fluorescence signals from a MB. The conjugation of MPA-AgNPs, MPA-AuNPs, CS MPA-Au/AgNPs, and alloyed MPA-AuAgNPs to GSH-CdSeS alloyed Qdots resulted in the formation of four different plasmonic NP-Qdot nanohybrids. Each of the nanohybrids were conjugated to the MB to form the respective plasmonic NP-Qdot-MB biosensor probe. The detection of low concentrations of ZIKV RNA was triggered only based on the LSPR-mediated fluorescence signal from the plasmonic NPs to the Qdots via the hybridization of the ZIKV RNA with the DNA oligonucleotide sequence of the MB. The LOD values for ZIKV RNA were in the following order: alloyed AuAgNP-Qdot646-MB > CS Au/AgNP-Qdot646-MB > AuNP-Qdot646-MB > AgNP-Qdot646-MB. We found that the bimetallic plasmonic NP-Qdots induced stronger LSPR-mediated fluorescence signals for ZIKV RNA detection than the single metallic plasmonic NP-Qdots. As a proof of concept, the Qdot-MB probe (without an LSPR signal) could not detect the ZIKV RNA at the concentration levels detected by the plasmonic NP-Qdot-MB biosensor probes, thus indicating that the LSPR signal from the plasmonic NPs influenced the detection sensitivity of the biosensor. Excellent specificity for ZIKV RNA was also exhibited by the plasmonic NP-Qdot-MB biosensor probes. The technique we have presented here provides a reliable detection platform which emphasizes the efficacy of LSPR-mediated fluorescence signal in a molecular beacon probe for rapid, ultrasensitive and specific ZIKV detection. However, the major limitation of our proposed detection platform is the cost effectiveness. We believe to meet the demand for point-of-care ZIKV diagnosis in low and middle income countries, low-cost detection platform are needed.

Appendix A. Supporting information

Supplementary data associated with this article can be found in the online version at doi:

References

Abushouk, A.I., Negida, A., Ahmed, H., 2016. J. Clin. Virol. 84, 53-58.

Adegoke, O., Nyokong, T., Forbes, P.B.C., 2015. Opt. Mater. 46, 548-554.

Adegoke, O., Park, E.Y., 2016. Nanoscale Res. Lett. 11:523.

Adegoke, O., Seo, M-S., Kato, T., Kawahito, S., Park, E.Y., 2016. J. Mater. Chem. B 4, 1489-1498.

Anker, J.N., Hall, W.P., Lyandres, O., Shah, N.C., Zhao, J., Van Duyne, R.P., 2008. Nat. Mater. 7, 442–453.

Balm, M.N., Lee, C.K., Lee, H.K., Chiu, L., Koay, E.S., Tang, J.W., 2012. J. Med. Virol. 84, 1501-1505

Barzon, L., Pacenti, M., Berto, A., Sinigaglia, A., Franchin, E., Lavezzo, E., Brugnaro, P., Palu, G., 2016. Eur. Surveill. 21, 2–6.

Calvet, G., Aguiar, R.S., Melo, A.S., Sampaio, S.A., de Filippis, I., Fabri, A., Araujo, E.S., de Sequeira, P.C., de Mendonca, M.C., de Oliveira, L., Tschoeke, D.A., Schrago, C. G.,

Thompson, F.L., Brasil, P., Dos Santos, F.B., Nogueira, R.M., Tanuri, A., de Fi- lippis, A.M., 2016. Lancet Infect. Dis. 16, 653-660.

Chen, H.M., Liu, R.S., Jang, L.Y., Lee, J.F., Hu, S.F., 2006. Chem. Phys. Lett. 421,118–123

Enfissi, A., Codrington, J., Roosblad, J., Kazanji, M., Rousset, D., 2016. Lancet 387 (10015) 227–228.

Fagbami, A.H., 1979. J. Hyg. (Lond) 83-213-219.

Faye, O., Diallo, D., Diallo, M., Weidmann, M., Sall, A.A., 2013. Virol. J. 10:311

Faye, O., Faye, O., Diallo, D., Diallo, M., Weidmann, M., Sall, A.A., 2013. Virol. J. 10, 310-311.

Gebre, Y., Forbes, N., Gebre, T., 2016. Asian Pac. J. Trop. Biomed. 6, 815-824.

Gourinat, A.-C., O'Connor, O., Calvez, E., Goarant, C., Dupont-Rouzeyrol, M., 2015. Emerg. Infect. Dis. 21, 84–86.

Hall, W.P., Ngatia, S.N., Van Duyne, R.P., 2011. J. Phys. Chem. C 115, 1410-1414.

Haug, C.J., Kieny, M.P., Murgue, B., 2016. N. Engl. J. Med. 374, 1802-1803.

Hutter, E., Pileni, M.-P., 2003. J. Phys. Chem. B 107, 6497–6499.

Kaszuba, M., Corbett, J., Watson, F.M., Jones, A., 2010. Philos. Transact. A Math. Phys. Eng. Sci. 368, 4439–4451.

Khan, M.A.M., Kumar, S., Ahamed, M., Alrokayan, S.A., AlSalhi, M.S., 2011. Nanoscale Res. Lett. 6:434.

Kindhauser, M.K., Allen, T., Frank, V., Santhana, R.S., Dye, C., 2016. Bull. World Health Organ. 171082, 1–18.

Lanciotti, R.S., Kosoy, O.L., Laven, J.J., Velez, J.O., Lambert, A.J., Johnson, A.J., Stanfield, S.M., Duffy, M.R., 2008. Emerg. Infect. Dis. 14, 1232–1239.

Law, W-C., Yong, K-T., Baev, A., Prasad, P.N., 2011. 5, 4858-4864.

Lazear, H.M., Diamond, M.S., 2016. J. Virol. 90, 4864–4875.

Li, T., Albee, B., Alemayehu, M., Diaz, R., Ingham, L., Kamal, S., Rodriguez, M., Bishnoi, SW., 2010. Anal. Bioanal. Chem. 398, 689–700.

Macnamara, F.N., 1954. Trans. R. Soc. Trop. Med. Hyg. 48, 139-45.

Marano, G., Pupella, S., Vaglio, S., Liumbruno, G.M., Grazzini, G., 2016. Blood Transfus. 14, 95–100.

Moore, D.L., Causey, O.R., Carey, D.E., Reddy, S., Cooke, A.R., Akinkugbe, F.M., David-West, T.S., Kemp, G.E., 1975. Ann. Trop. Med .Parasitol. 69, 49-64.

Musso, D., Nhan, T., Robin, E., Roche, C., Bierlaire, D., Zisou, K., Yan, A.S., Cao-Lormeau, V.M., Broult, J., 2014. Eur. Surveill. 19, 6–8.

Olson, J.G., Ksiazek, T.G., Suhandiman, T., 1981. Trans. R. Soc. Trop. Med. Hyg. 75, 389-393.

Pan, D., Wang, Q., Jiang, S., Ji, X., An, L., 2007. J. Phys. Chem. C 111, 5661-5666.

Pardee, K., Green, A.A., Ferrante, T., Cameron, D.E., DaleyKeyser, A., Yin, P., Collins, J.J., 2014. Cell 159, 940–954.

Patel, V.R., Agrawal, Y.K., 2011. J. Adv. Pharm. Technol. Res. 2, 81–87.

Petersen, L.R., Jamieson, D.J., Powers, A.M., Honein, M.A., 2016. N. Engl. J. Med. 374, 1552–1563.

Rademeyer, P., Carugo, D., Lee, J.Y., Stride, E., 2015. Lab Chip 15, 417–428.

Sharma, B., Rabinal, M.K., 2015. J. Alloy Compd. 649, 11-18.

Sikka, V., Chattu, V.K., Popli, R.K., Galwankar, S.C., Kelkar, D., Sawicki, S.G., Stawicki, S.P., Papadimos, T.J., 2016. J. Glob. Infect. Dis.8, 3–15.

Slot, J.W., Gueza, H.J., 1988. Method Microbiol. 20, 211–236.

Thompson, J.D., Gibson, T.J., Plewniak, F., Jeanmougin, F., Higgins, D.G., 1997. Nucl. Acids Res. 10, 4876–4882.

Waggoner, J.J., Gresh, L., Mohamed-Hadley, A., Ballesteros, G., Davila, M.J.V., Tellez, Y., Sahoo, M.K., Balmaseda, A., Harris, Eva., Pinsky, B.A., 2016. Emerg. Infect. Dis. 22, 1295–1297.

World Health Organization. Director-General summarizes the outcome of the emergency committee regarding clusters of microcephaly and Guillain-Barré syndrome. http://www.who.int/mediacentre/news/statements/ 2016/emergency-committee-zika-microcephaly/en/; 2016. [Accessed on 9th December, 2016].

World Health Organization. Emergencies: the history of Zika virus. Geneva: World Health Organization; 2016. [Online] Available from: http://www.who.int/emergencies/zika-virus/timeline/en/ [Accessed on 9th December, 2016].

Figure legends

Scheme 1. The conjugation of the plasmonic NPs to GSH-CdSeS Qdots (Qdot646) to form the plasmonic NP-Qdot nanohybrids; the subsequent conjugation of the plasmonic NP-Qdots to the MB to form the plasmonic NP-Qdot-MB biosensor probe and the LSPR-mediated fluorescence signal detection of the ZIKV based on hybridization of the RNA with the DNA loop sequence of the MB.

Fig. 1. UV/vis absorption spectra of the MPA-capped plasmonic NPs (A), size-dependent GSH-capped Qdots (B) and fluorescence spectra of the different-sized Qdots (C).

Fig. 2. TEM images and corresponding particle size distribution histograms of (A, A1) MPA-capped AgNPs, (B, B1) MPA-capped AuNPs, (C, C1) MPA-capped CS Au/AgNPs, (D, D1) MPA-capped alloyed AuAgNPs and (E, E1) Qdot646 nanocrystals.

Fig. 3. PXRD spectra of the plasmonic NPs (A) and Qdot646 nanocrystals (B).

Fig. 4. DLS plot and corresponding ZP plots of (A, A1) MPA-capped AgNPs, (B, B1) MPA-capped AuNPs, (C, C1) MPA-capped CS Au/AgNPs, (D, D1) MPA-capped alloyed AuAgNPs and (E, E1) Qdot646 nanocrystals.

Fig. 5. TEM images of the plasmonic NP-Qdot nanohybrids: (A) AgNP-Qdot646, (B) AuNP-Qdot646, (C) CS Au/AgNP-Qdot646 and (D) alloyed AuAgNP-Qdot646; and plasmonic NP-Qdot-MB: (A1) AgNP-Qdot646-MB, (B1) AuNP-Qdot646-MB, (C1) CS Au/AgNP-Qdot646-MB and (D1) alloyed AuAgNP-Qdot646-MB.

Fig. 6. (A) Fluorescence quenching effect of the plasmonic NPs on the fluorescence of Qdot646 particles. (B − E) LSPR-mediated fluorescence enhancement of ZIKV RNA using the plasmonic NP-Qdot-MB biosensor probe, (B) AgNP-Qdot646-MB, (C) AuNP-Qdot646-MB,

(D) CS Au/AgNP-Qdot646-MB and (E) alloyed AuAgNP-Qdot646-MB. Inset: structure of the plasmonic NP-Qdot-MB biosensor probe.

Fig. 7. Fluorescence calibration curve for ZIKV RNA detection showing the LSPR-mediated fluorescence signal of the (A) AgNP-Qdot646-MB, (B) AuNP-Qdot646-MB, (C) CS Au/AgNP-Qdot646-MB and (D) alloyed AuAgNP-Qdot646-MB. Error bars represent standard deviation of 3 replicate measurements.

Fig. 8. Selectivity of the plasmonic NP-Qdot-MB biosensor probe toward ZIKV RNA in the presence of the negative controls (influenza virus (IV) H3N2 and norovirus (NV)). (A) AgNP-Qdot646-MB, (B) AuNP-Qdot646-MB, (C) CS Au/AgNP-Qdot646-MB and (D) alloyed AuAgNP-Qdot646-MB. Error bars represent standard deviation of 3 replicate measurements.
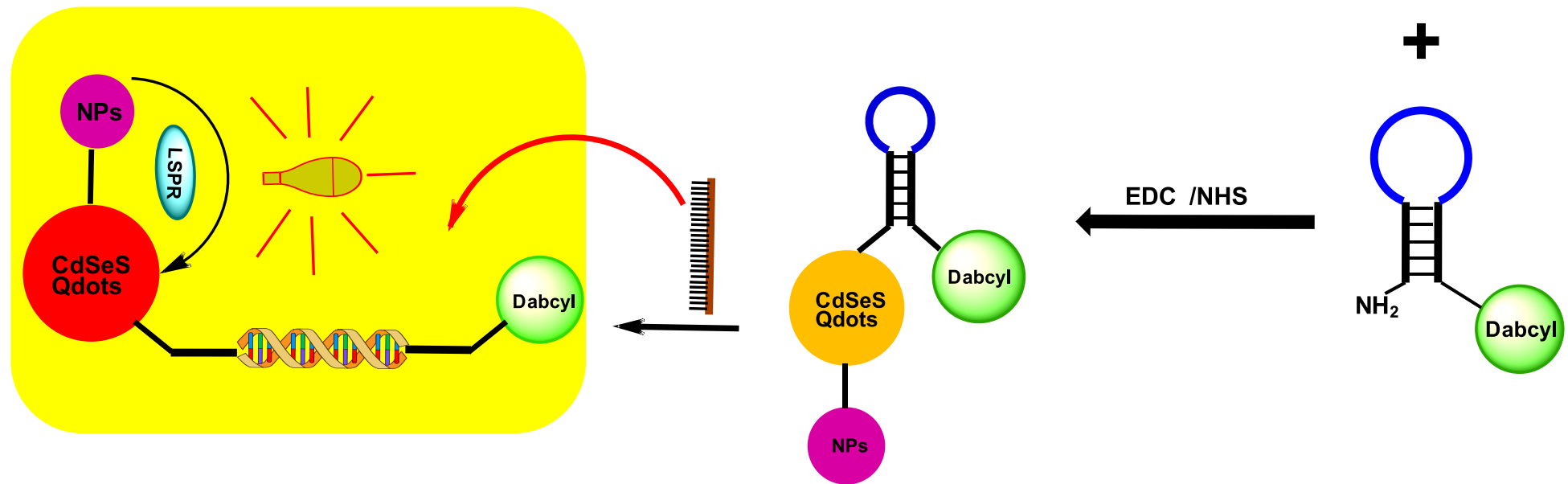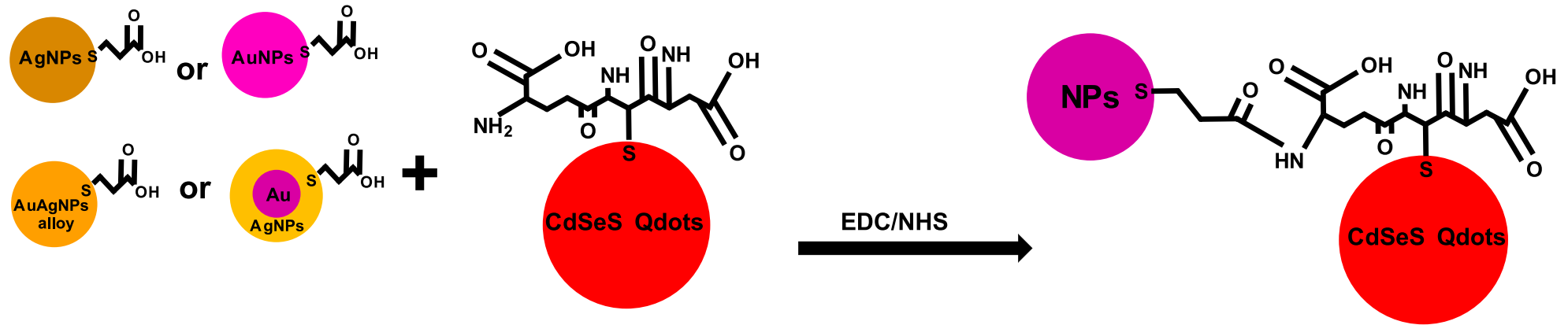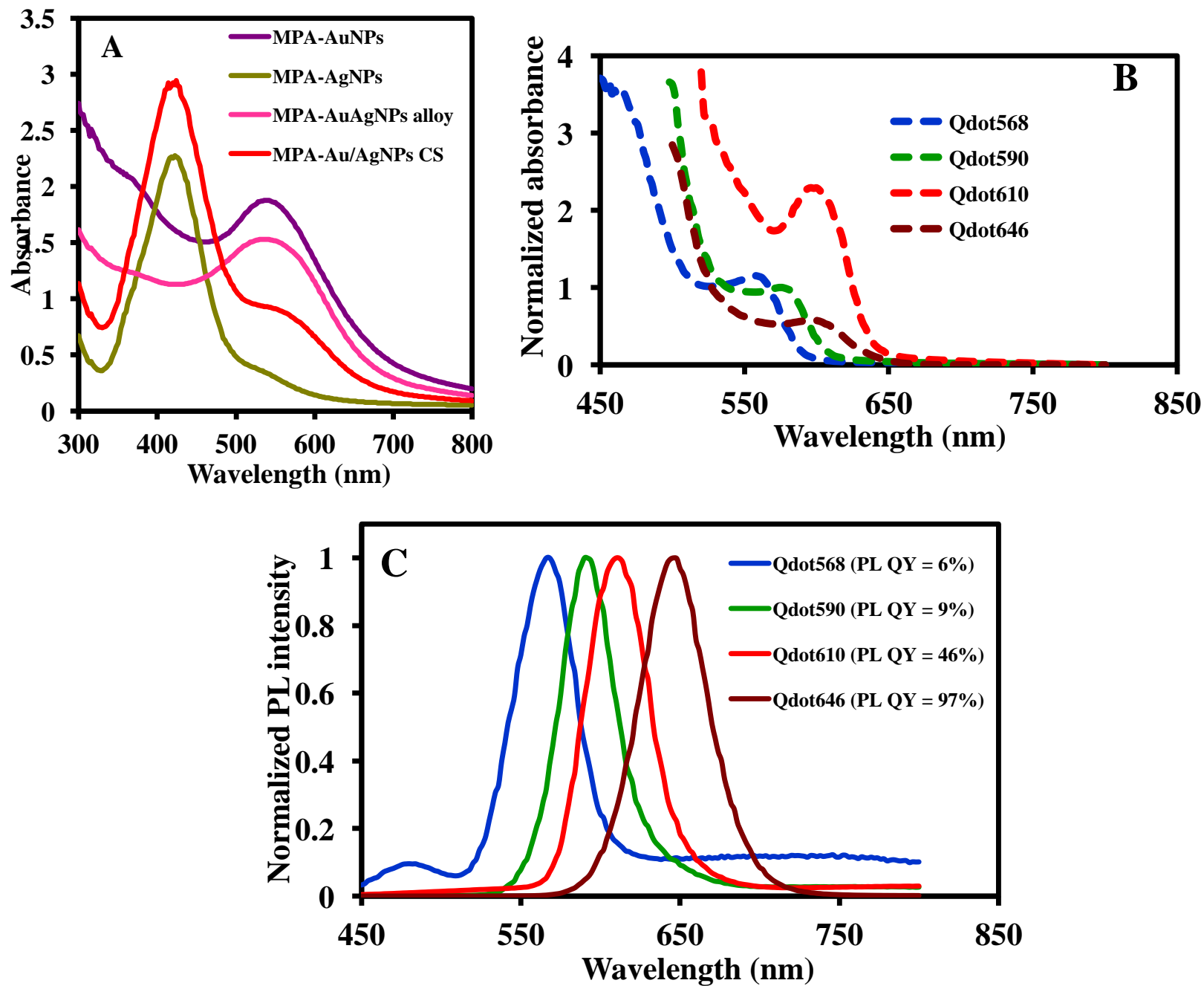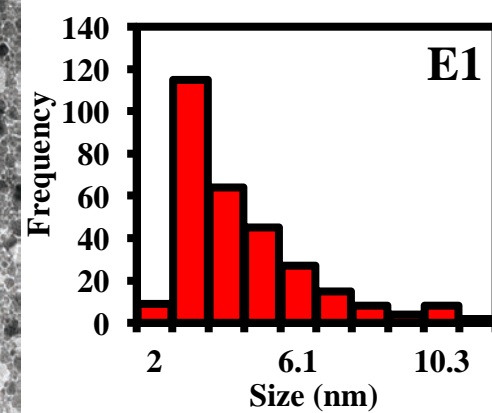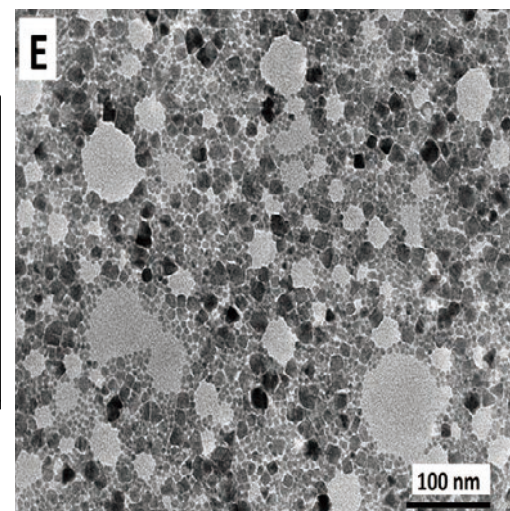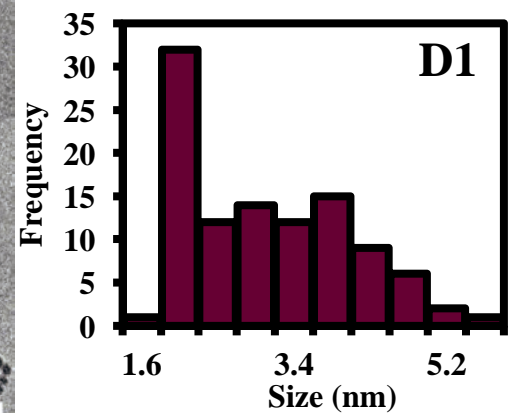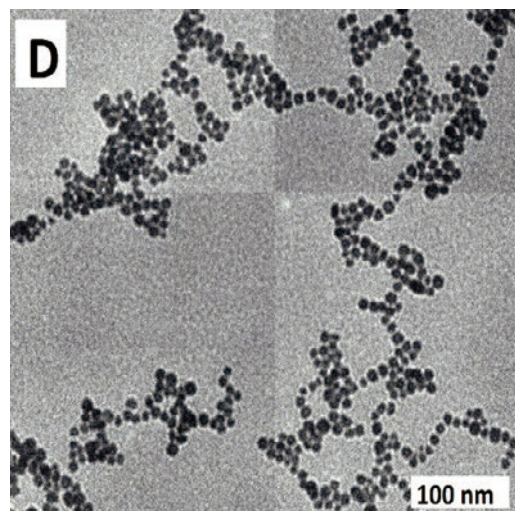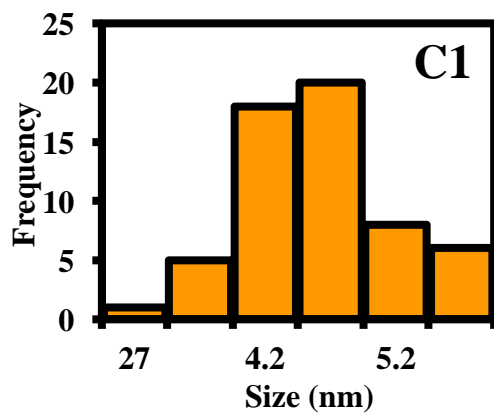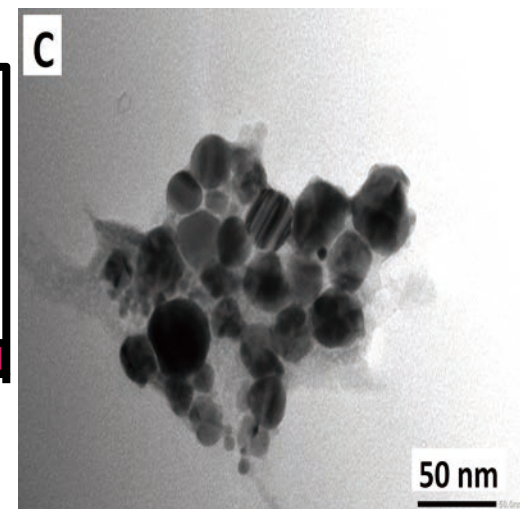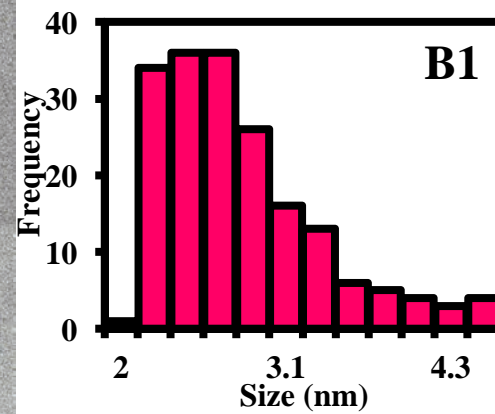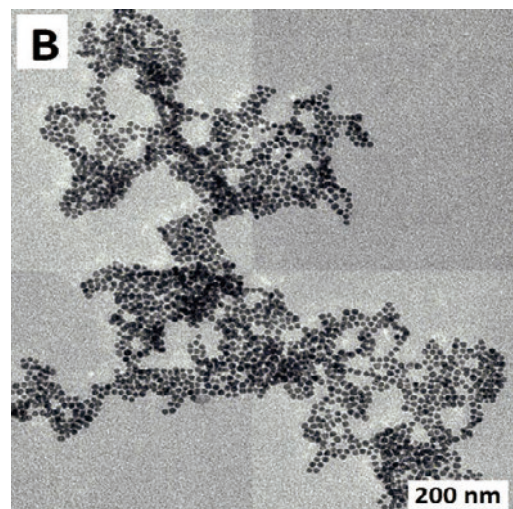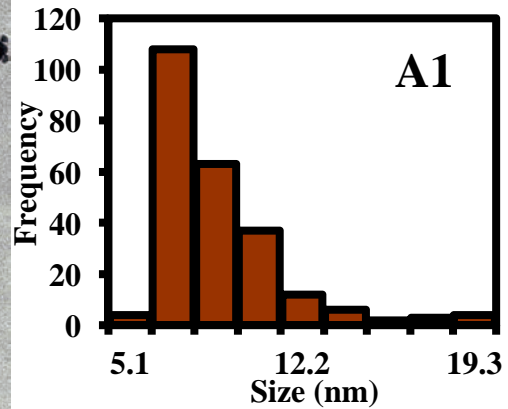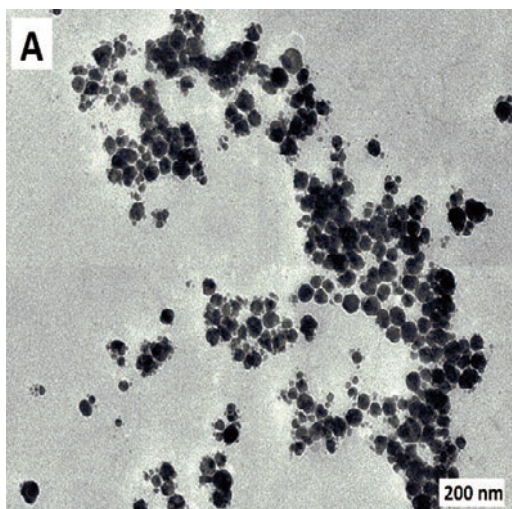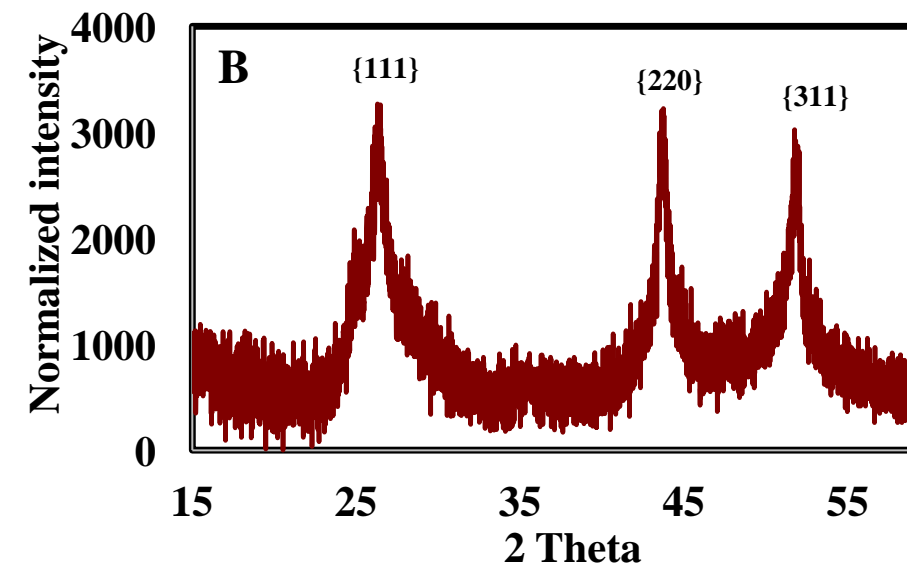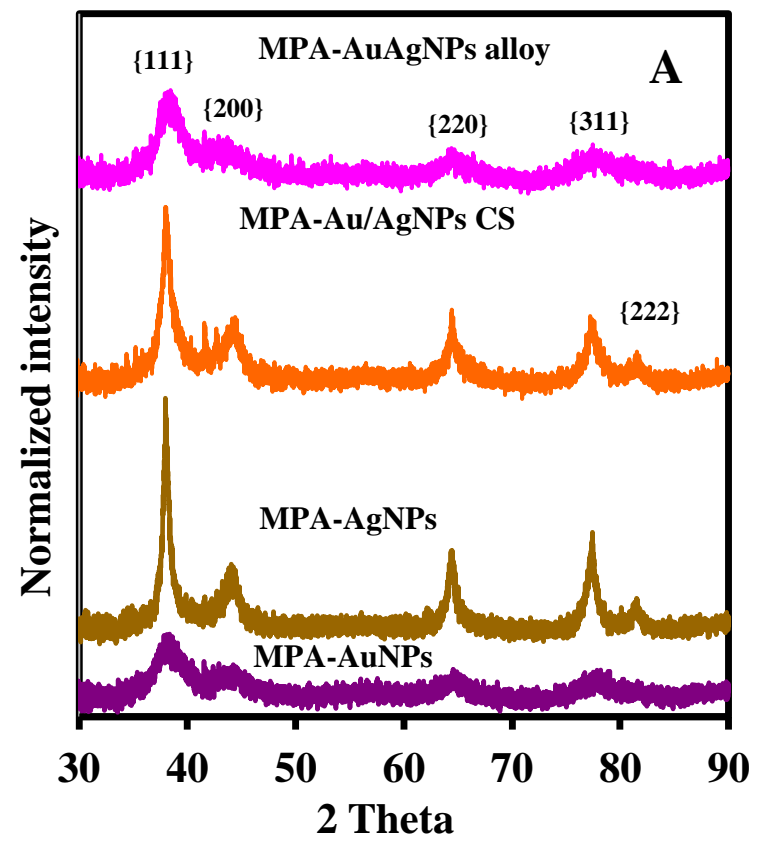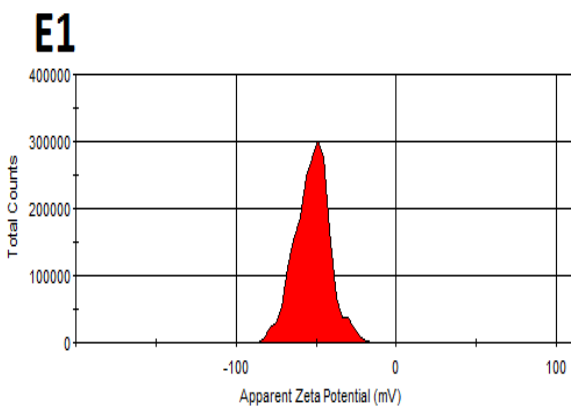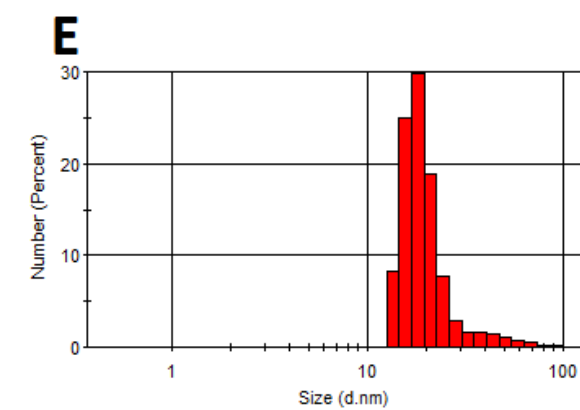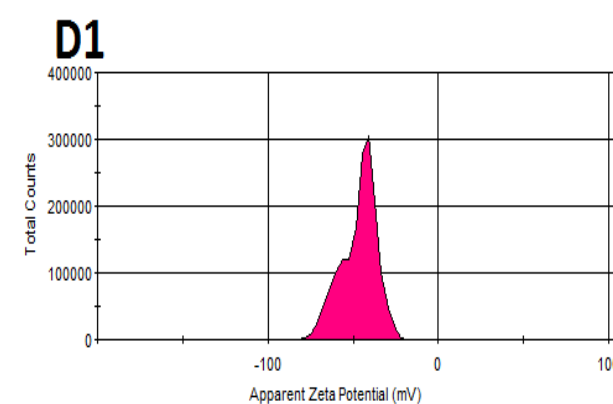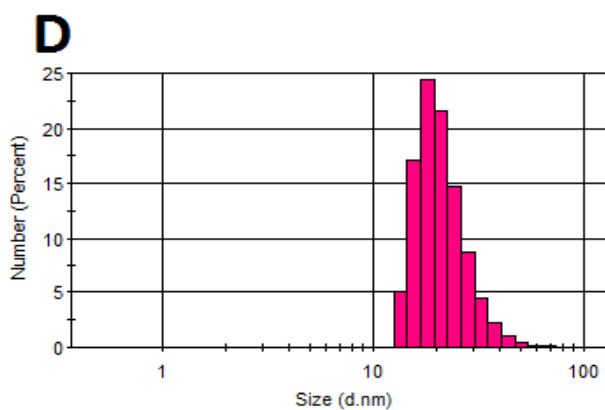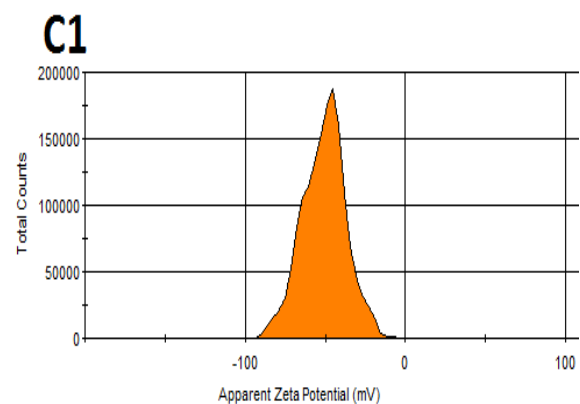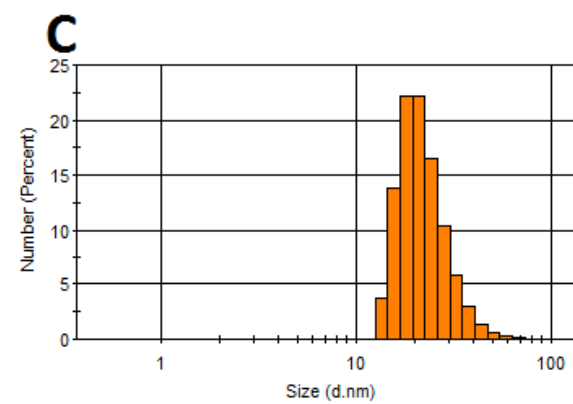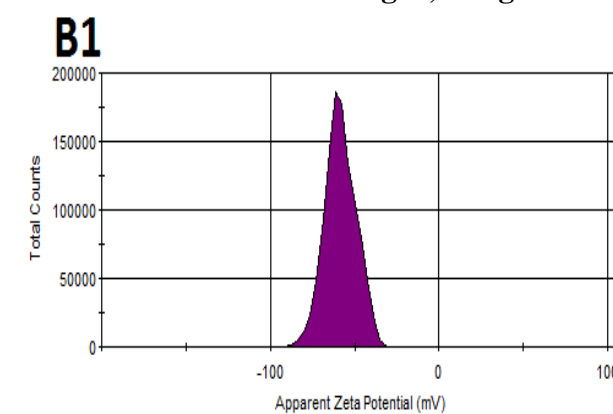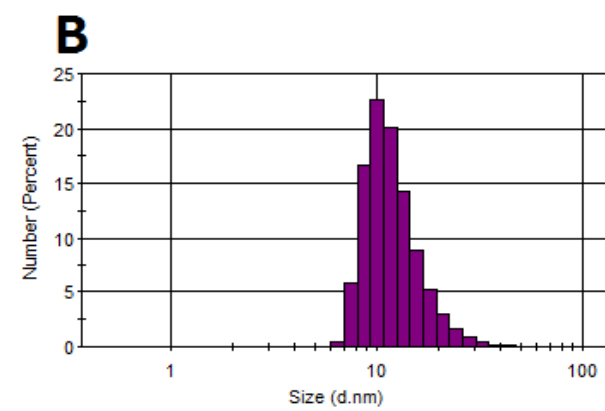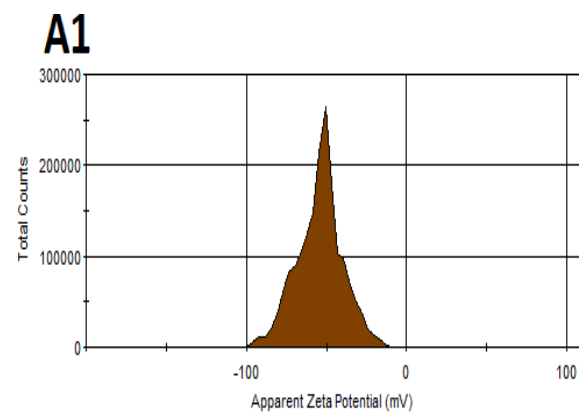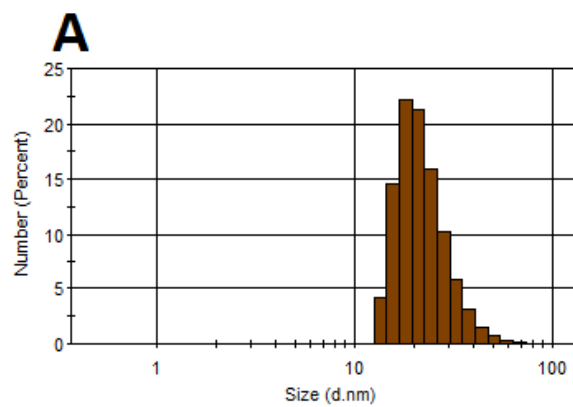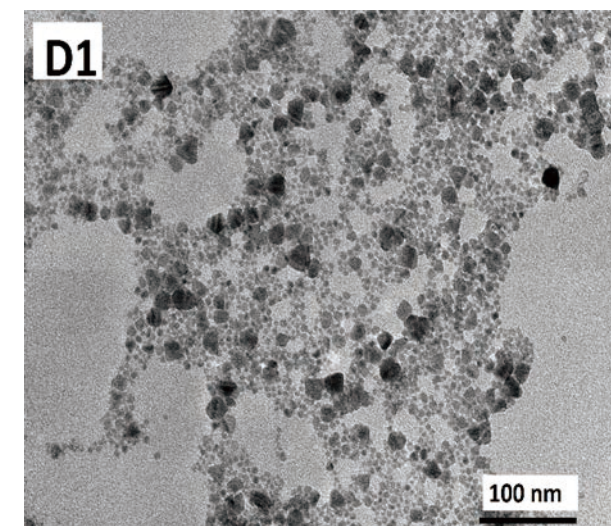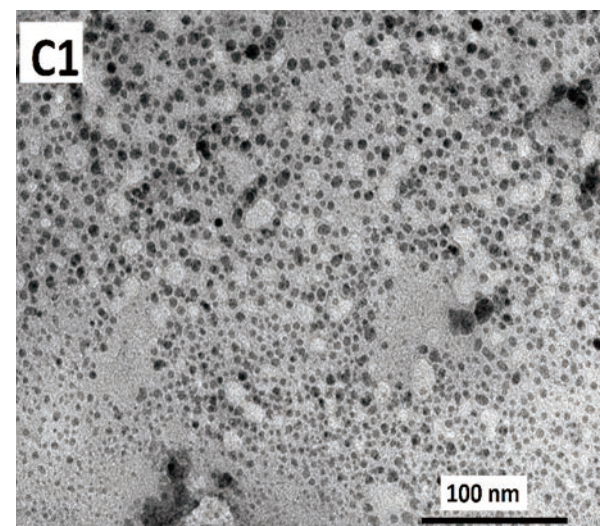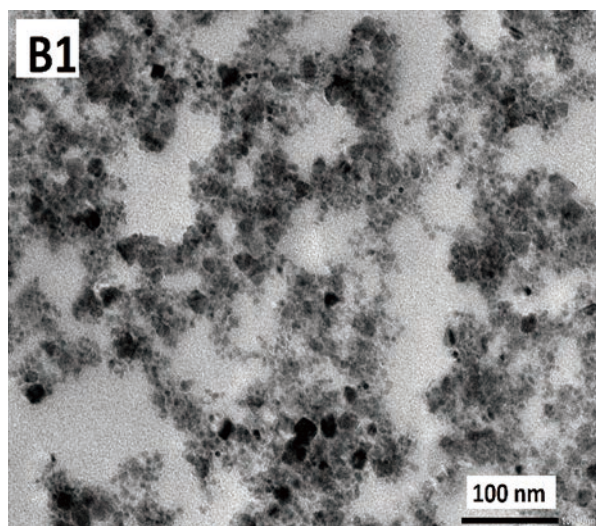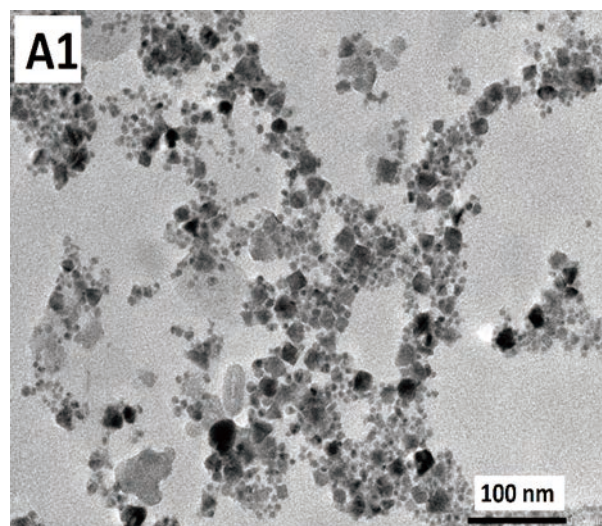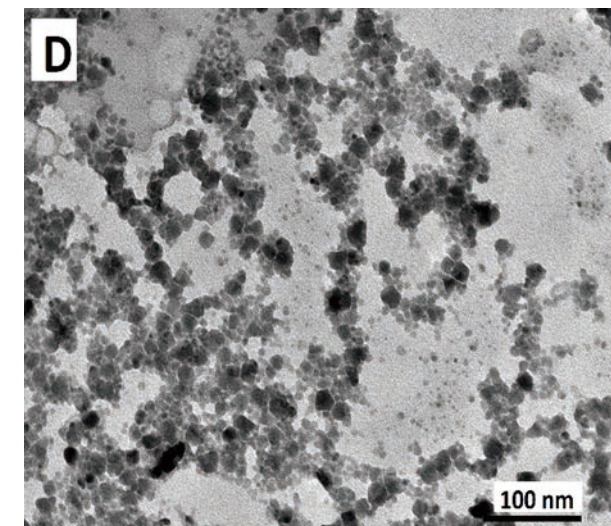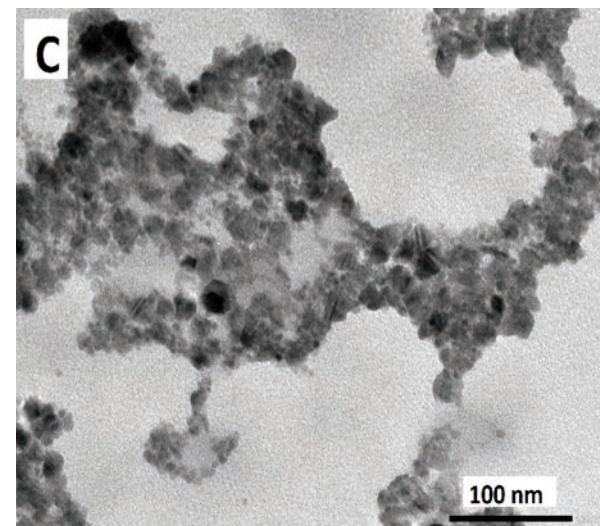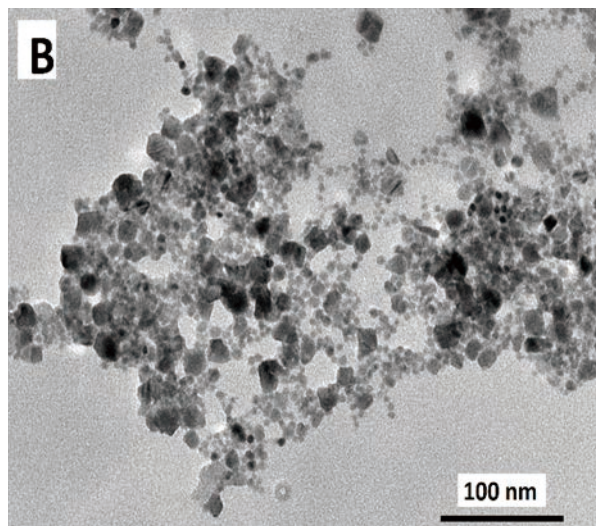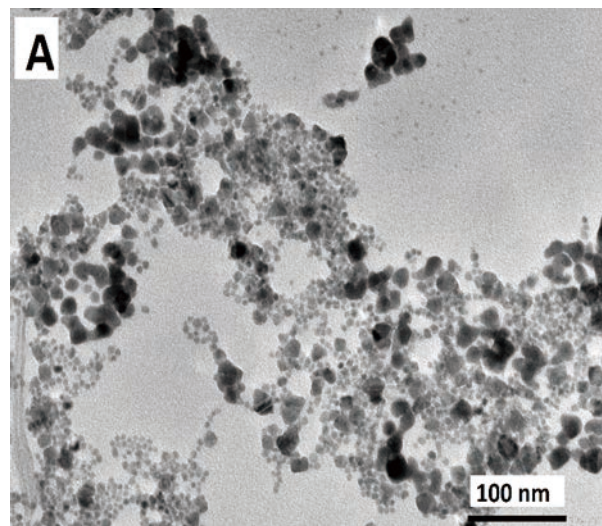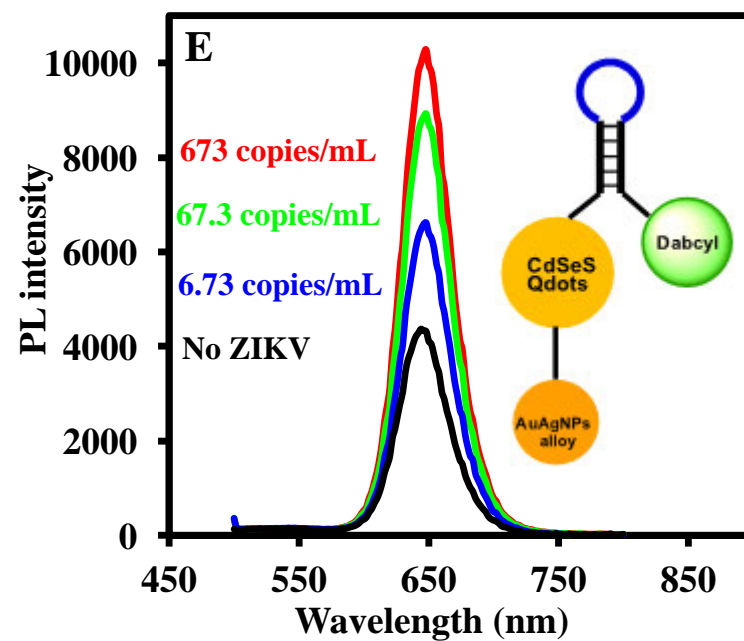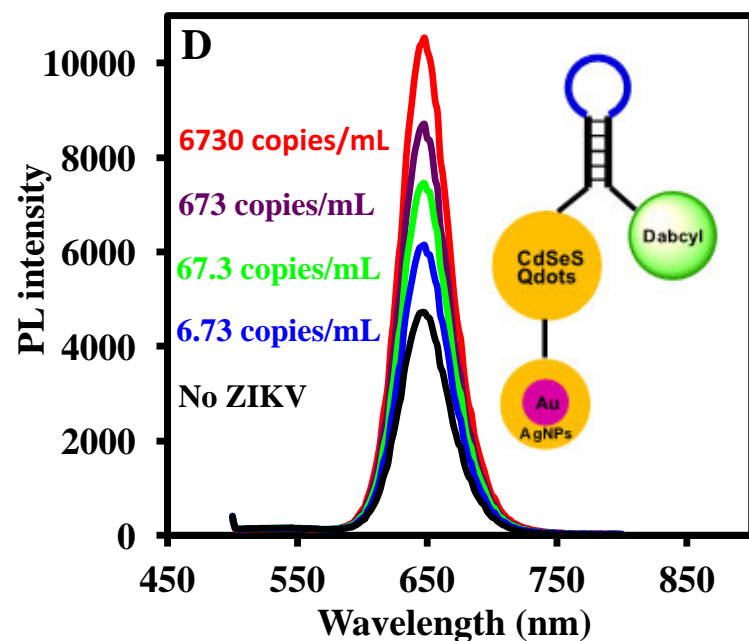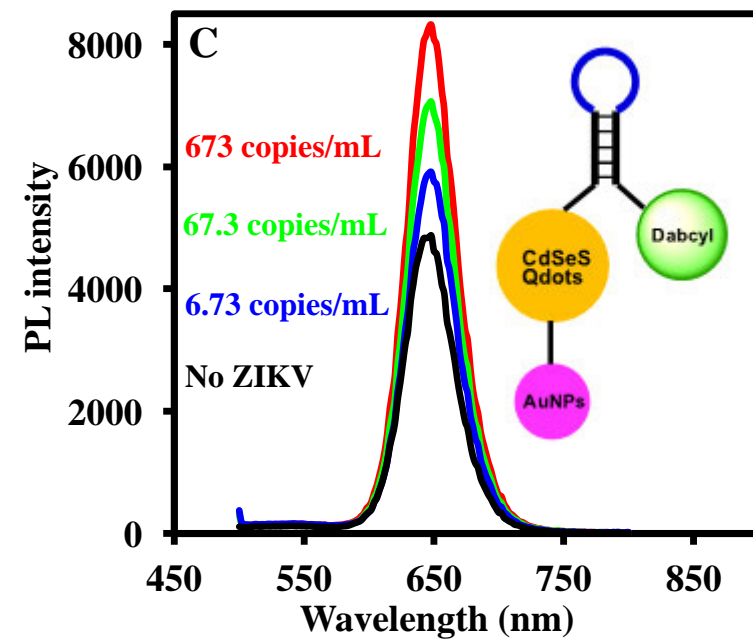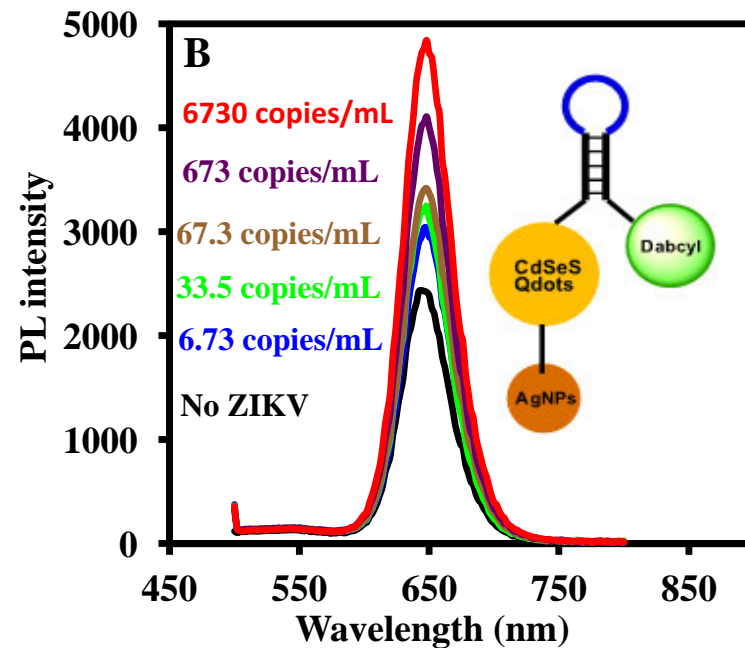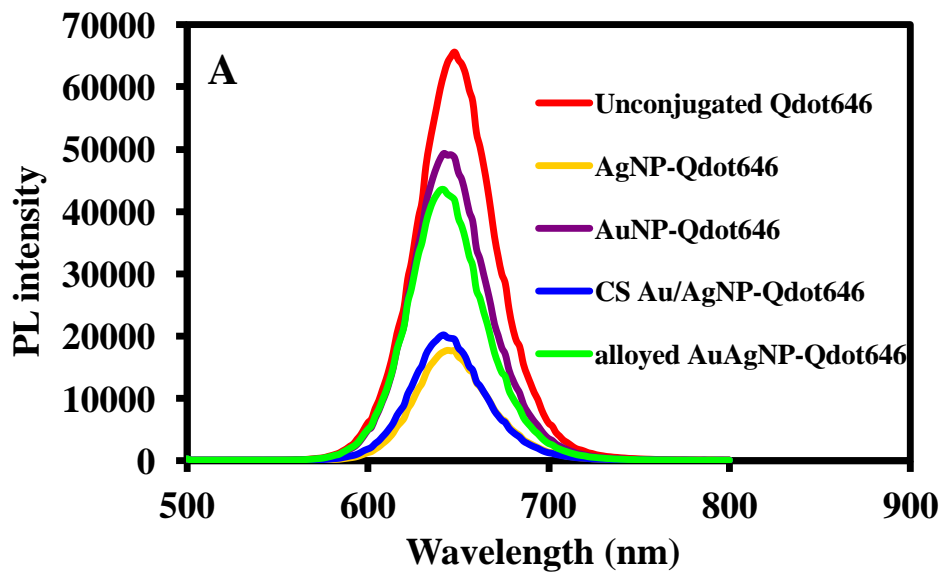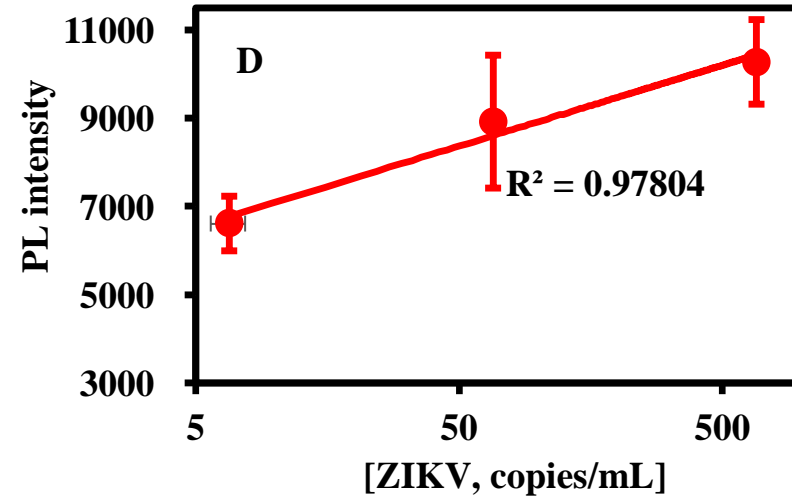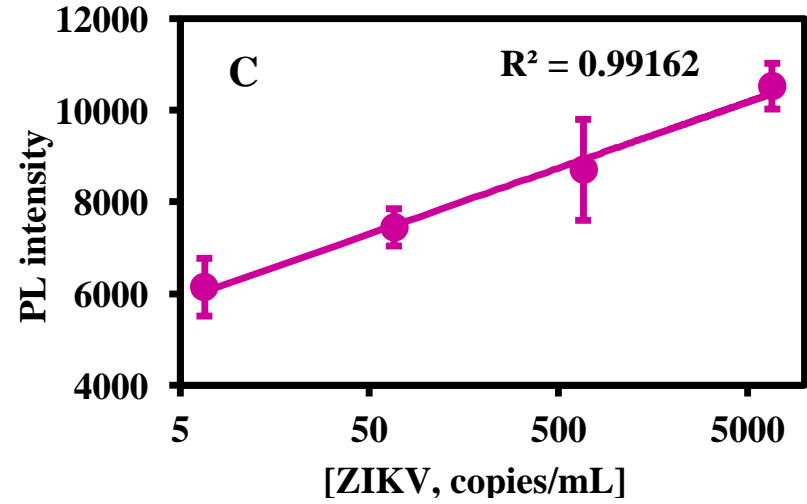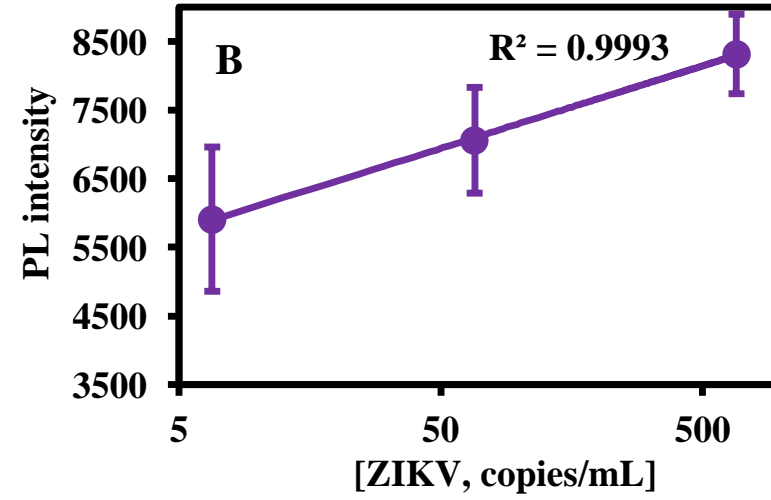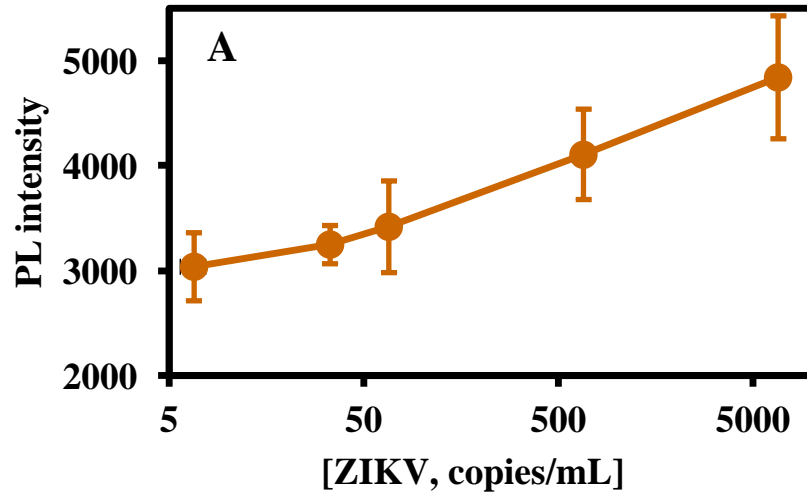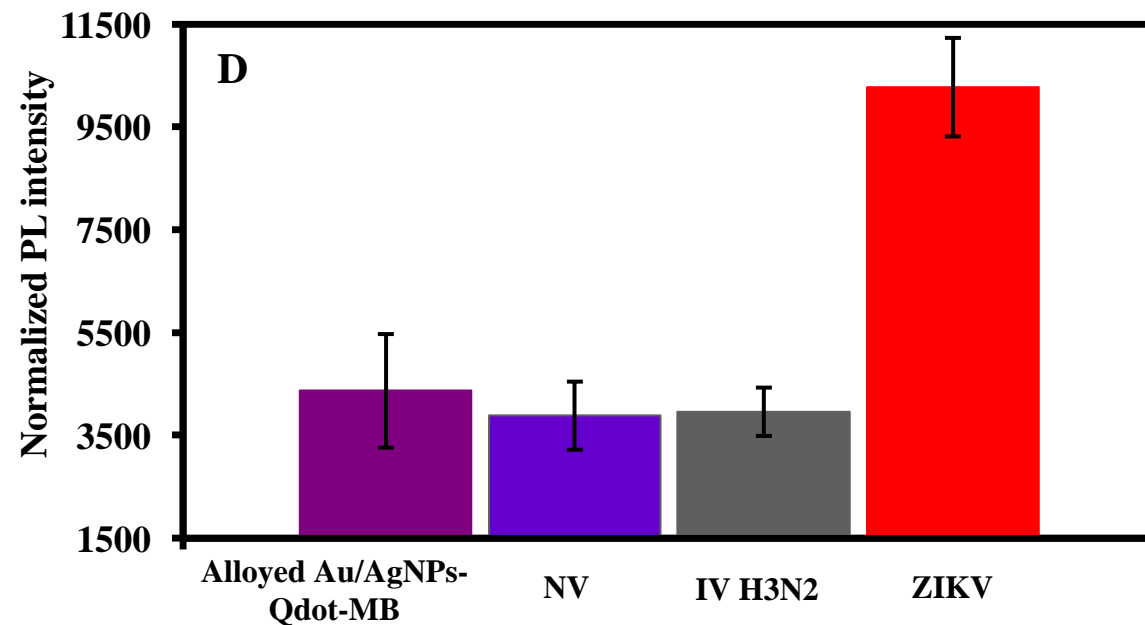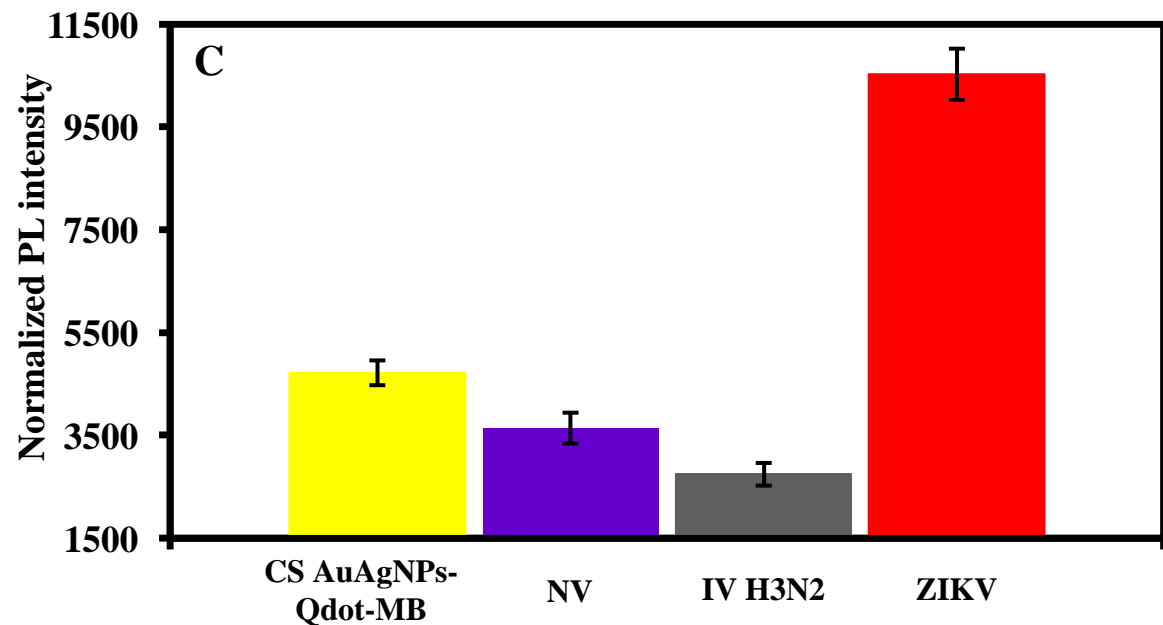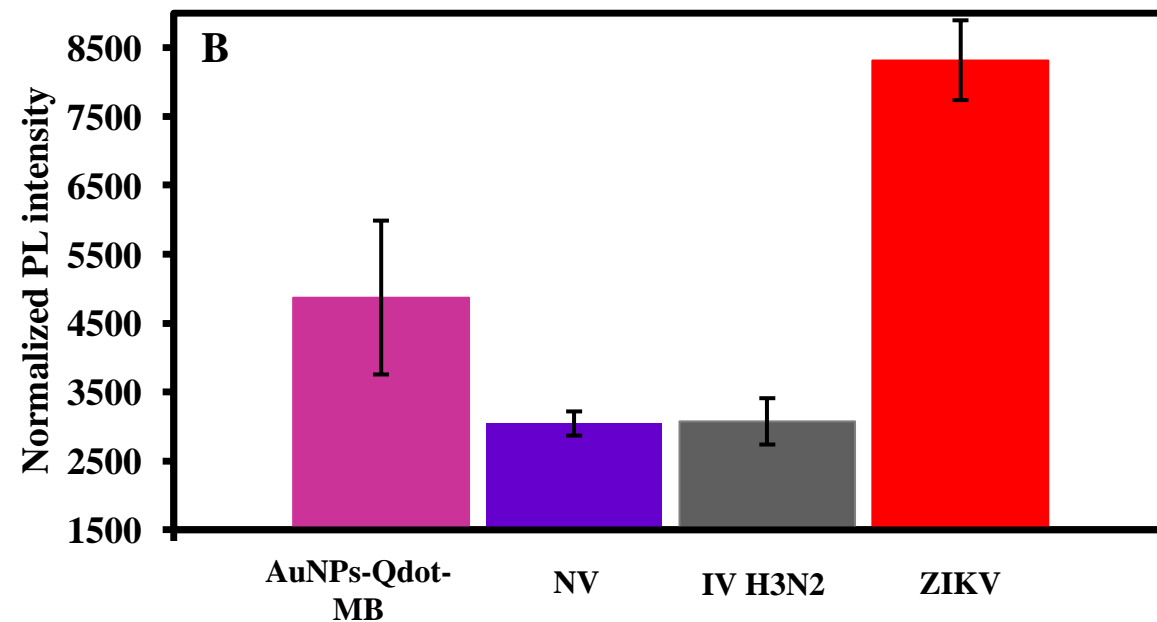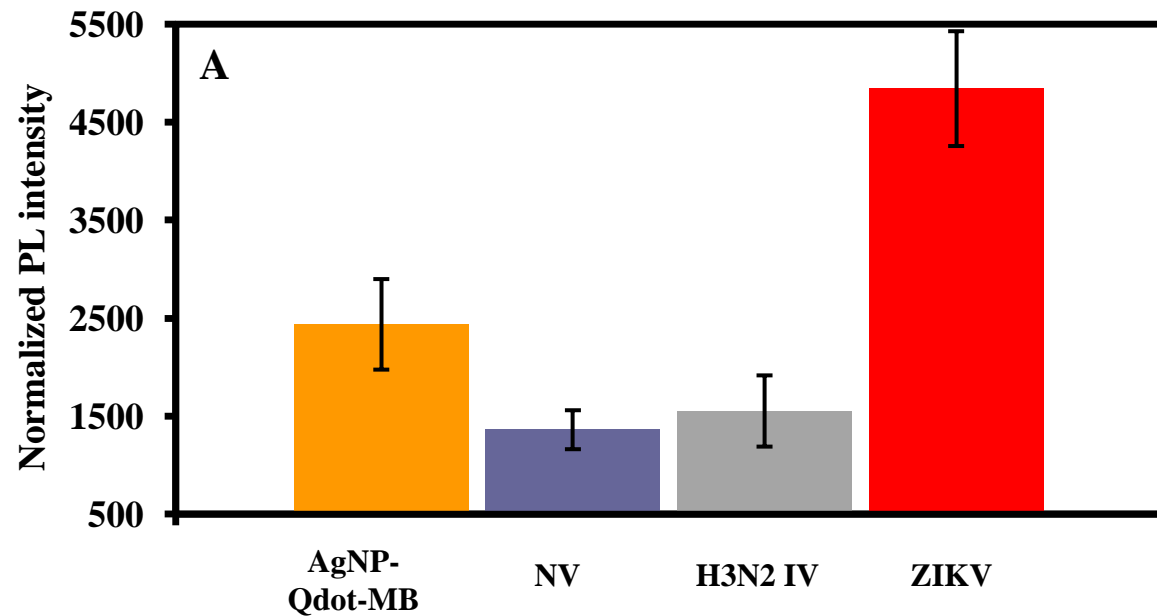
Supporting Information

Localized surface plasmon resonance-mediated fluorescence signals in plasmonic nanoparticle-quantum dot hybrids for ultrasensitive Zika virus RNA detection via hairpin hybridization assays

Oluwasesan Adegoke[a], Masahiro Morita[b], Tatsuya Kato[a,b,d], Masahito Ito[c], Tetsuro Suzuki[c], Enoch Y. Park[a,b,d*]

[a] *Laboratory of Biotechnology, Research Institute of Green Science and Technology, Shizuoka University, 836 Ohya, Suruga-ku, Shizuoka 422-8529, Japan*

[b] *Department of Applied Biological Chemistry, Shizuoka University, 836 Ohya, Suruga-ku, Shizuoka 422-8529, Japan*

[c] *Department of Virology and Parasitology, Hamamatsu University School of Medicine, 1-20-1 Higashi-ku, Handa-yama, Hamamatsu 431-3192, Japan*

[d] *Laboratory of Biotechnology, Graduate School of Science and Technology, Shizuoka University, 836 Ohya, Suruga-ku, Shizuoka 422-8529, Japan*

E-mail addresses:
adegoke.sesan@mailbox.co.za (OA)
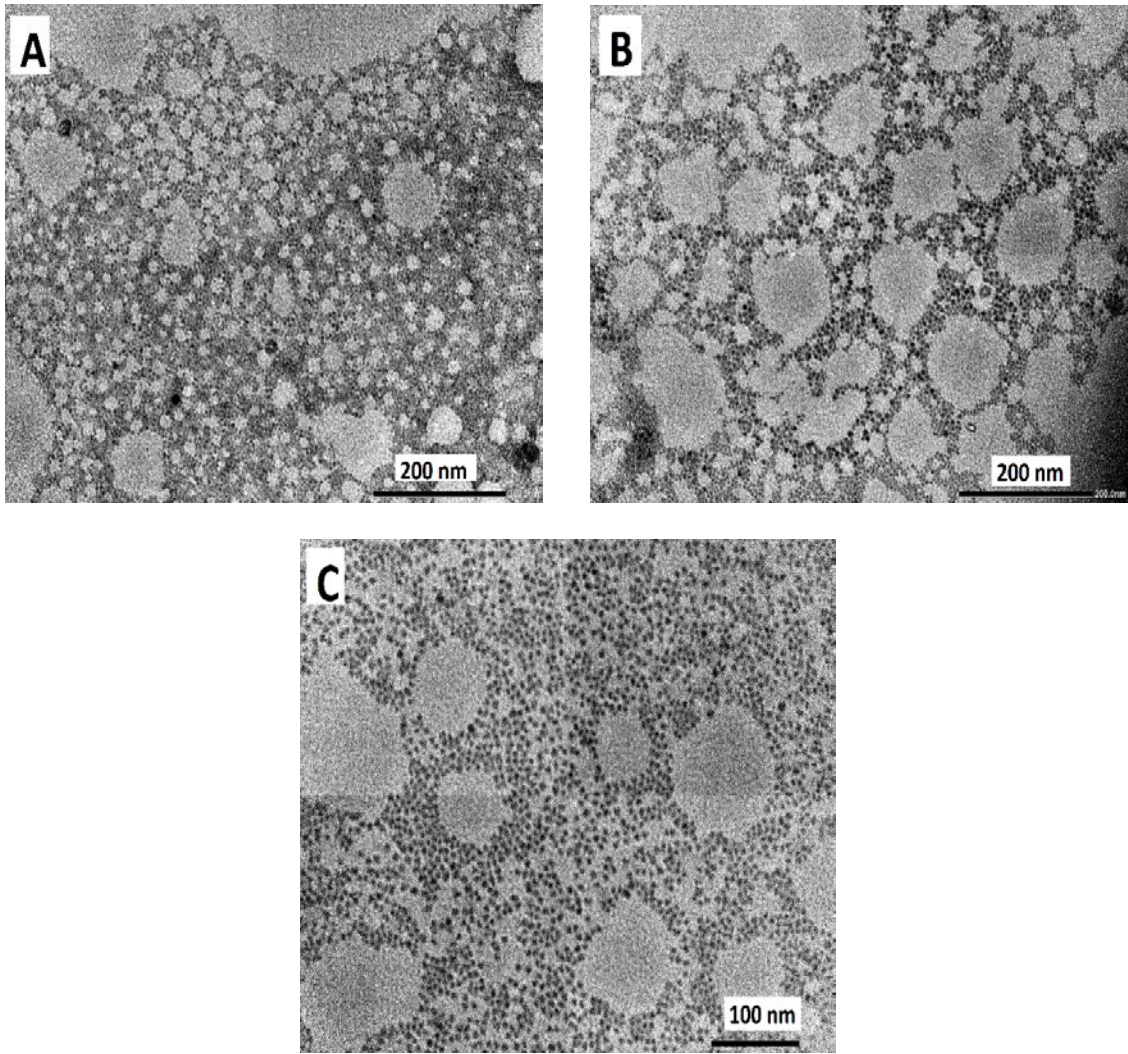nnndrum@yahoo.co.jp (MM)
tesuzuki@hama-med.ac.jp (TS)
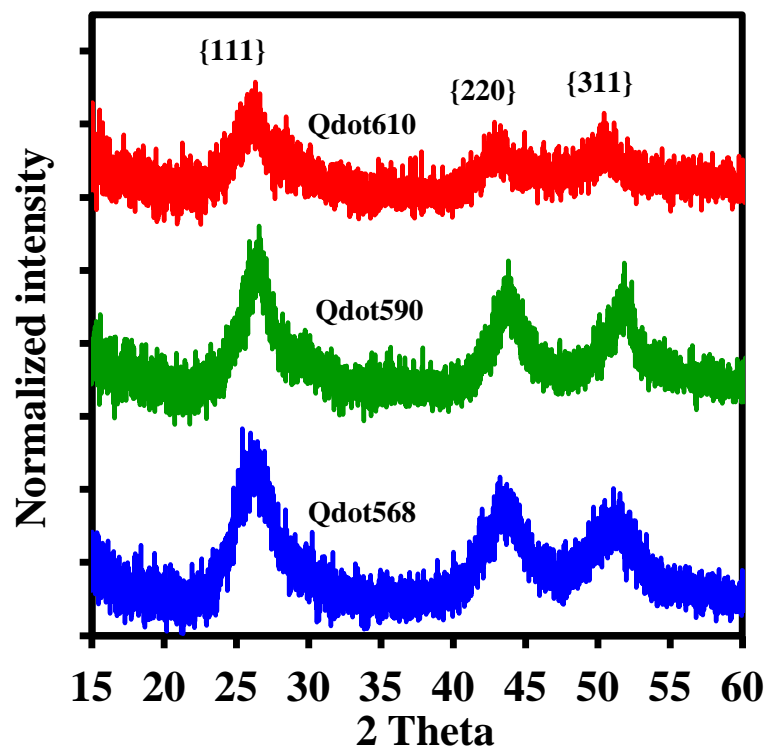mito557@hama-med.ac.jp (MI)
tesuzuki@hama-med.ac.jp (TS)
park.enoch@shizuoka.ac.jp (EYP)

[*] Correspondence to: Research Institute of Green Science and Technology, Shizuoka University, 836 Ohya Suruga-ku, Shizuoka, 422-8529, Japan. Tel. & fax: +81 54 238 4887. *E-mail address:* park.enoch@shizuoka.ac.jp (EYP)
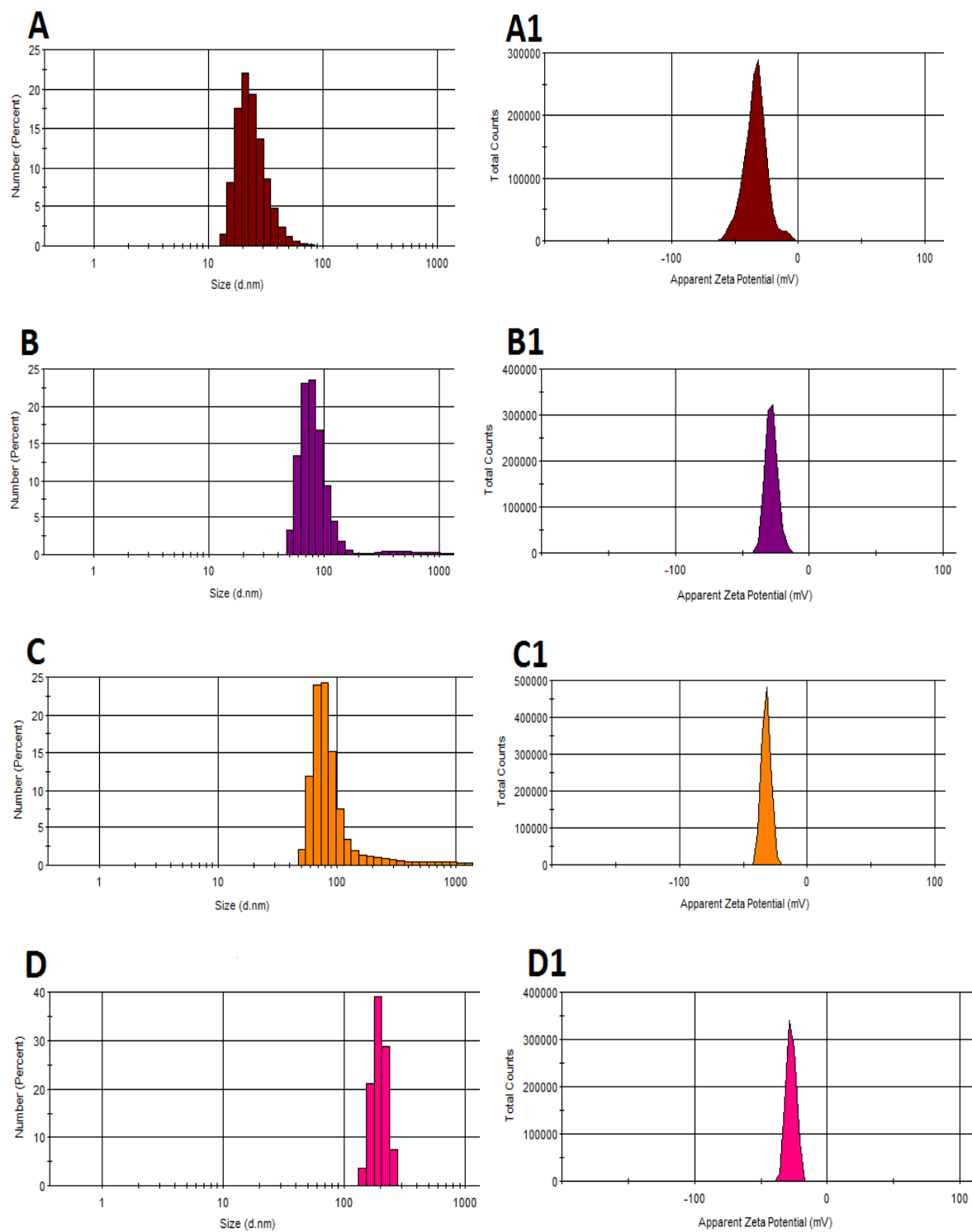
**Fig. S-1.** TEM images of GSH-capped Qdot568, Qdot590 and Qdot610.

**Fig. S-2.** PXRD spectra of the GSH-capped Qdot568, Qdot590 and Qdot610.

Fig. S-3. DLS and ZP plot of (A,A1) AgNPs-Qdot646, (B,B1) AuNPs-Qdot646, (C,C1) CS Au/AgNPs-Qdot646 and (D,D1) alloyed AuAgNPs-Qdot646.

The DLS and ZP plots for the plasmonic NP-Qdot-MB are shown in Fig. S-4. The values obtained are 26.6±8.1 nm; -31.8±9.2 mV for AgNPs-Qdot646-MB, 34.9±13.0 nm; -30.4±5.0 mV for AuNPs-Qdot646-MB, 35.4±12.1 nm; -32.2±10.6 mV for CS Au/AgNPs-Qdot646-MB and 35.7±13.1 nm; -33.0±5.8 mV for alloyed AuAgNPs-Qdot646-MB. The hydrodynamic values indicate that the binding of the MB to the plasmonic-NP-Qdot triggered a better dispersion of the particles and did not induce aggregation. The ZP values indicate high colloidal stability for the respective plasmonic NP-Qdot-MB conjugates.
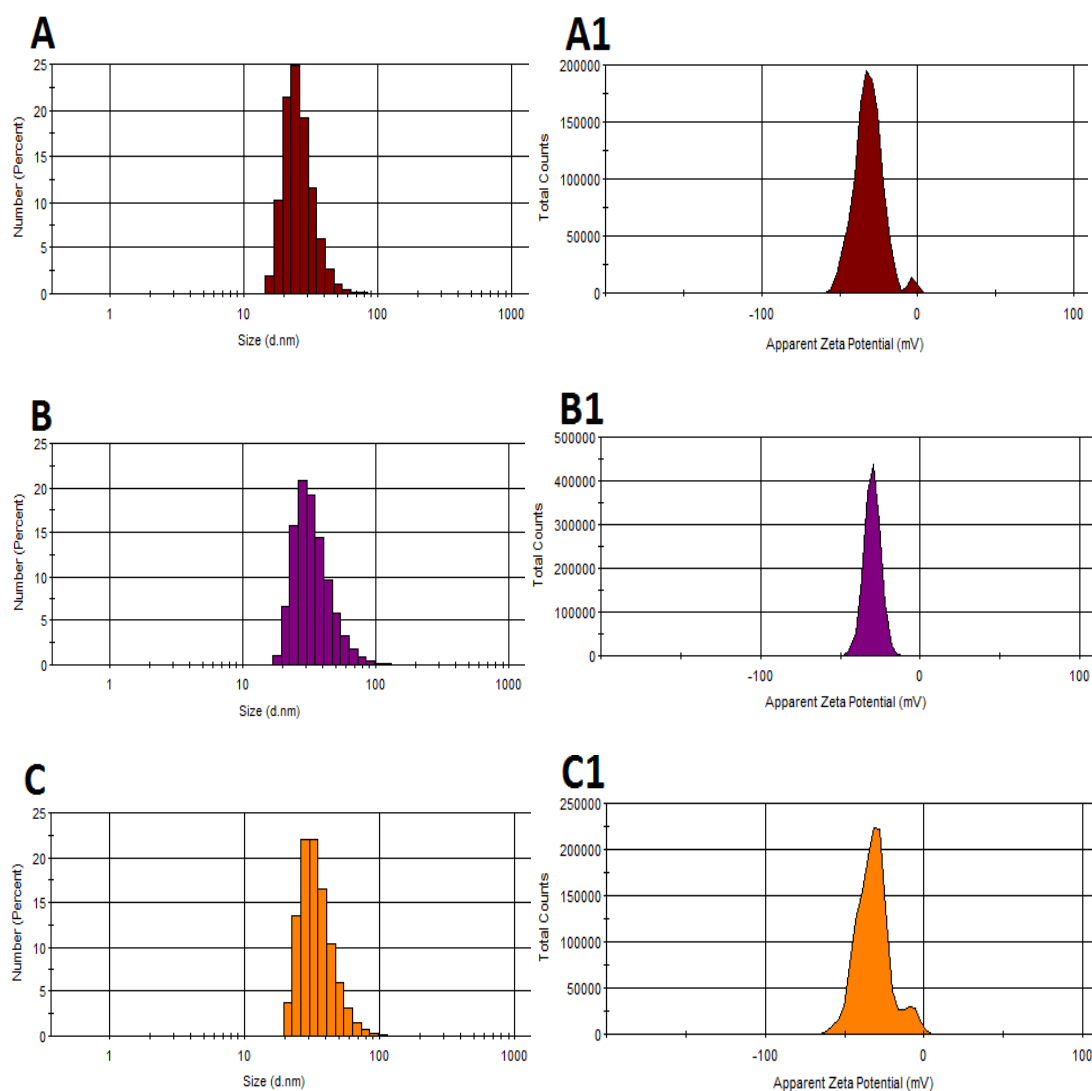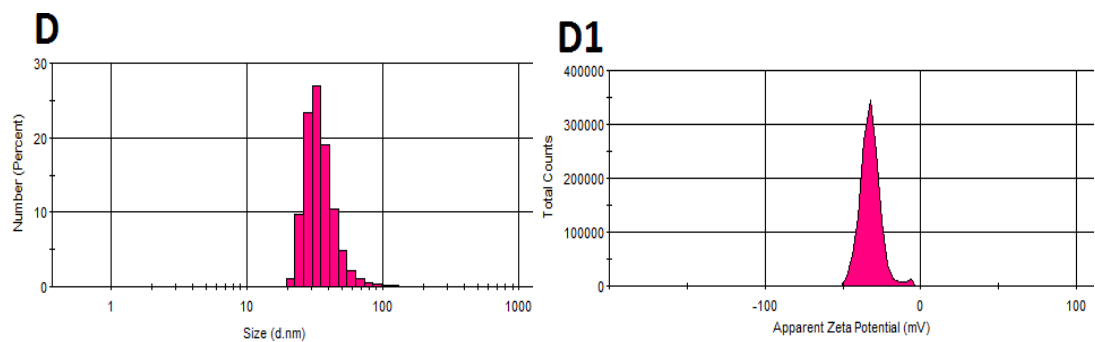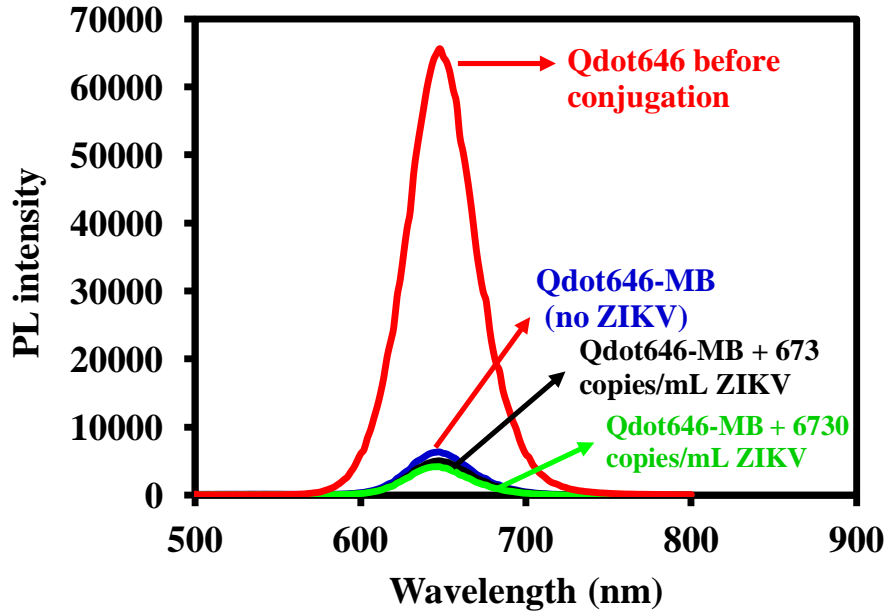
Fig. S-4. DLS and ZP plot of (A,A1) AgNPs-Qdot646-MB, (B,B1) AuNPs-Qdot646-MB, (C,C1) CS Au/AgNPs-Qdot646-MB and (D,D1) alloyed AuAgNPs-Qdot646-MB.
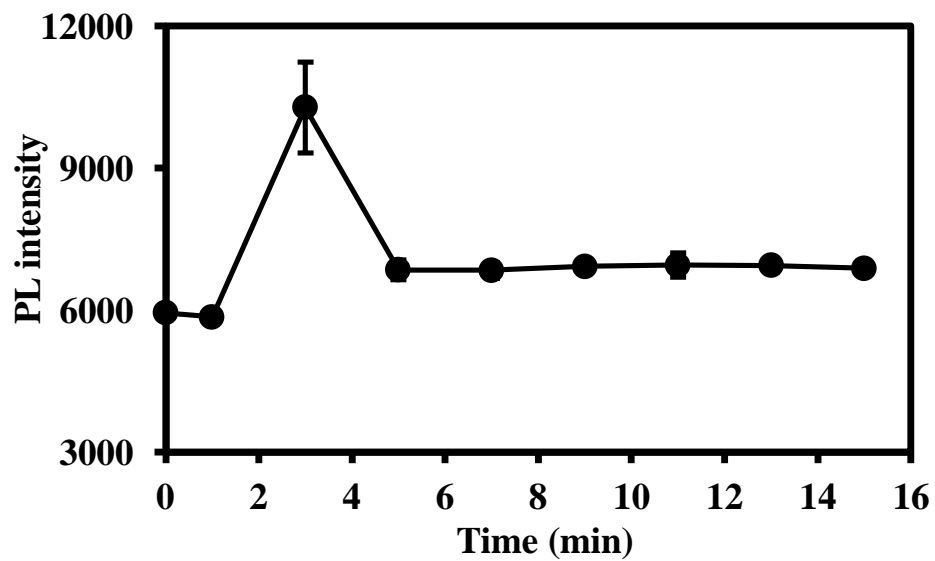
Fig. S-5. Time-lapse hybridization time of alloyed AuAgNPs-Qdot646-MB in the presence of 673 copies/mL of ZIKV. Error bars represent standard deviation of 3 replicate measurements.

Fig. S-6. Fluorescence spectra of Qdot646 before conjugation to the MB (red line), after conjugation to the MB (Qdot646-MB) (blue line), Qdot646-MB + 673 copies/mL of ZIKV (black line) and Qdot646-MB + 6730 copies/mL of ZIKV (green line) The plot shows that Qdot646-MB cannot detect ZIKV.